AN *IN-SITU* STAGE FOR SCRATCHING INSIDE ESEM AND ON SCRATCHING OF GLASS

By
SANJAI SRIRANGAPATANA KESHAVAN
Bachelor of Engineering
Mysore University
Chitradurga, India
1990

Submitted to the faculty of the
Graduate College of the
Oklahoma State University
in partial fulfillment of
the requirements for
the Degree of
MASTER OF SCIENCE
December, 1994

AN *IN-SITU* STAGE FOR SCRATCHING INSIDE ESEM AND ON SCRATCHING OF GLASS

Thesis Approved:

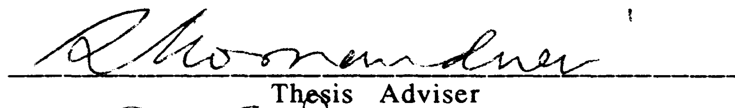

Thesis Adviser

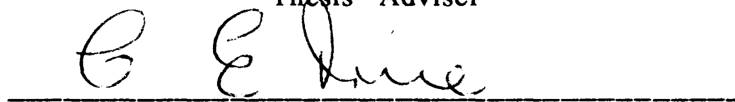

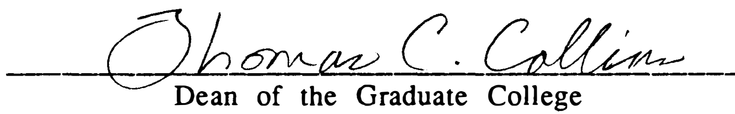

Dean of the Graduate College

PREFACE

The production of optical quality glass surfaces involves two steps. First, the surface has to be ground with a fixed abrasive (grinding) for the production of macro geometry. This is followed by polishing with loose abrasives for obtaining micro geometry. From an economic and contour accuracy standpoints of glass finishing it appears advantageous to minimize polishing and obtain as good a surface as possible by just grinding. However, it is difficult to obtain the required finish using conventional grinding machines. A new generation of precision machines are evolving to meet this need. When brittle materials are ground at light loads ($\approx$ 1 N) and low depths of cut even though the material removal mechanism may be brittle, the resulting cracks may not grow to a stage where they become large scale microcracks. Hence, the process is termed as 'gentle' or 'microcrackfree' grinding. The critical features in the development of ultraprecision machines are thermal stability, vibration isolation, kinematic support, feed back controls and metrology frames. In addition to these, the economic manufacture of precision parts made of advanced ceramics and glasses hinges on an understanding of the mechanics of the material removal process.

There has been a significant interest recently on grinding/ scratching of various brittle materials such as ceramics, glasses, germanium, etc. without producing large scale microcracks [3-10,17,18]. However, the actual mechanisms of microcrackfree grinding/scratching are not well established. Various theories have been putforth by researchers, some of which are listed in the following:

1. Densification effect owing to the high hydrostatic pressure present at the tip of the tool.

2. Plastic flow similar to that occuring in metals.

3. Viscoplastic flow, due to the interface temperatures in grinding reaching values above the glass transition [Tg] temperature. Even many ceramics, such as silicon nitride, contain glassy phases due to the presence of sintering agents present during their processing.

4. The smooth grooves formed are due to heavy microcracking ahead of the tool and the surface is damaged only if the microcracks penetrate inside the bulk material. i.e there is no 'ductile regime' material removal of ceramics.

5. For brittle materials with glassy phase, the smooth grooves are generated does not necessarily mean that the surfaces are generated by plastic deformation, but can be due to viscoplastic flow when the interface temperatures exceeds the glass transition [Tg] temperature. Also, in submicron machining of glasses, the radius of the tool forms a high negative rake angle, so the stresses induced may be sufficient enough to deform the material plastically.

The primary aim of this investigation is to design and build an ultraprecision *in-situ* stage for scratching inside an environmental scanning electron microscope (ESEM) and study the mechanism of the material removal in glass.

For simplicity, initially the stage of the ESEM was used to mount the workpiece and the force transducer. The depth of cut was given by the X- axis motion of the stage and cutting motion by the Y- axis of the stage. The tool was held stationary below the ESEM detector on the microinjector shaft. Scratching force was measured by a 3-axis piezoelectric dynamometer and read by a digital multimeter. The motion of the stage was controlled externally by a CPU transition module, RS 232, and VT 100. This setup unfortunately did not function satisfactorily because the tool was not rigid enough and

would deflect from the detector's view even when low loads were applied.

In the second design the tool was mounted on a rigid stationary tool holder while retaining the rest of the system. In this set up, it was possible to make the desired scratches. But, inspite of many trials, it was not possible to bring the tool under the beam. Each time the position of the tool is changed, the chamber has to be vented, which is time consuming and not a good practice, as it may damage the vacuum system in the long run. The design was again modified to overcome this problem.

In the third design, an independent scratching unit was built and the stage of the ESEM was used for positioning the tool below the beam. The machine is capable of giving depths of cut in the micrometric range up to a maximum 15 μm., when scratching at velocities from 0.143 to 0.5 mm/sec. Scratching force was measured by a dynamometer mounted behind the tool. The depth of cut is given by a piezo actuator controlled by a piezo controller. The cutting motion is provided by a dc motor, an ultraprecision linear slide, and a precision ball screw assembly. To and fro motion of the workpiece is obtained by changing the polarity of the input current. With this design, the motor and piezo actuator can be controlled from outside the chamber. Also, the tool adjustment can be done without disrupting the vacuum. *In-situ* scratching experiments were performed and recorded in a video type recorder. The minimum requirements for performing *in-situ* experiments were then established.

Cutting experiments were performed using a conical diamond indenter with a tip radius of ≈16 μm , at very small depths of cuts(≈1 μm). The specimen, after scratching, was also viewed in the SEM, for finer details after coating it with gold palladium. Experiments were conducted varying the normal load and velocity (minimum and maximum velocities achievable by the equipment, and minimum

possible normal load (≈0.03N) and average load for obtaining grooves with surface damage (≈0.15N).

Smooth grooves were formed for low load experiments and cracks were produced at higher loads. But, at higher loads, there were also stretches on the groove where the material was removed due to fracture and the groove was not damaged. At low loads, a side flow was observed, and at higher loads this side flow separates as a long continuous chips. At low loads, formation of groove involves flow of material and densification on the groove surface directly below the indenter. At higher loads, groove formation involves brittle fracture, flow of material, chip formation and densification on the groove surface directly below the indenter. The material flow and chip formation process could not be observed *in-situ* due to a process limitation, material flow being blocked by the scratching tool itself.

ACKNOWLEDGMENT

I would like to thank Dr. R. Komanduri for guiding me through out the investigation. Without his guidance and help I would not have been able to complete this investigation. Sincere thanks extend to my other two committee members, Dr. C. E. Price and Dr. D. Lucca.

I would also like to thank those who have provided suggestions and assistance for this investigation: Dr. T. Ram Mohan, P. S. Ravi, H. Murali, D. Subramanyan, Johnie Hixon, B. Shekar, M. Raghunandan K. Mallika and Kishor A.

The project was supported by a grant from OCAST- MOST Chair and ARPA Ceramic Bearing Technology program. I would like to thank Drs. W. Coblenz of ARPA and K. Mecklenburg of WPAFB for their interest.

TABLE OF CONTENTS

Chapter		Page
I.	INTRODUCTION	1
II.	GLASS	
	Glass definition and structure	4
	Network modifiers	4
	Machining of glass	6
III.	LITERATURE REVIEW	
	Review of indentation scratching experiments	9
IV.	DESIGN AND FABRICATION OF *IN-SITU* SCRATCHING STAGE INSIDE ESEM	
	Considerations for the design of the *in-situ* scratching stage inside ESEM	29
	Requirements of scratching apparatus	33
	First design	33
	Force measuring circuit	35
	Second design	36
	Third design	38
V.	EXPERIMENTAL PROCEDURE AND TEST RESULTS	42
VI	DISCUSSIONS	59
VII	CONCLUSIONS	62
VIII	RECOMMENDATIONS FOR FUTURE WORK	64
	APPENDICES	
A1	ESEM	69

A2 Details of components used in scratching apparatus 72

LIST OF TABLES

Table		Page
2.1	Chemical and physical properties of soda lime silica glass	7
3.1	Effect of tool rake angle on critical depth after Blake and Scatterwood [7]	24
3.2	Effect of surface cutting speed on critical depth after Blake and Scatterwood [7]	24
5.1	Cutting conditions inside ESEM for 115° cone angle	43
5.2	Cutting conditions outside ESEM for 115° cone angle	43
5.3	Cutting conditions inside ESEM for 75° cone angle	46
5.4	Cutting conditions outside ESEM for 75° cone angle	52
A2.1	Specifications of piezo translator	83
A2.2	Specifications of piezo controller	84
A2.3	Specifications of dynamometer	86
A2.4	Specifications of ultra precision linear slide	88
A2.5	Specifications of precision ball screw assembly	88

LIST OF FIGURES

Figure		Page
1.1	Material removal mechanisms due to brittle fracture after Evans and Marshall [2]-------------------------	2
2.1	Tetrahedral arrangement of SiO_4 [11]---------------	5
2.2	Structure of pure silica glass [11]---------------------	5
2.3	Structure of silica glass with network modifiers [12]-	6
2.4	Microgrinding regime after Miyashata [47] ---------	8
3.1	Indentations produced on an extra dense flint glass after Taylor [13]--------------------------	10
3.2	Plastic indentations on soda glass and steel produced by vickers indenter after Marsh [5]-------	11
3.3	Scratches produced by trailing of a hard point over a glass after Marsh [5]------------------------	11
3.4	Profile of ball indentation on plate glass after Peter [16]--	13
3.5	Specific grinding energies during grinding with diamond and silicon carbide [17] -------------------	14
3.6	Proposed model for loose abrasive grinding (a) brittle (b) ductile and (c) glass flow after Golini and Jacob [18]--	16
3.7	Scratching apparatus developed by Van Groenou and veldkamp [20]--------------------------------------	17
3.8	Surface as a parameter of applied load and velocity.	

	after Goneru and Veldkamp [20]---------------------	18
3.9	Schematic diagram of scratching set up after Schinker [9]---	19
3.10	Long thin chips, at 100 m/sec scratching speed after Schinker [9] ---------------------------------------	20
3.11	Schematic diagram of scratching setup after Puttick [8]----------------------------------- -------	21
3.12	Spiral swarf adhering machined grooves in spectrosil. after Puttick [8] -------------------------------------	22
3.13	PAUL after Blake and Scatterwood [7]---------------	23
3.14	Mechanism for microcrack free machining after Blake and Scatterwood [7]--------------------------	23
3.15	Effect of tool rake angle on critical dept [7] ----------	24
3.16	Effect of tool clearance angle on critical depth after Blake and Scatterwood [7]--------------------------	25
3.17	Schematic of grinding apparatus after Bifano [22]----	26
3.18	Brittle ductile transition as a function of grinding infeed rate for fused silica after Bifano [22]---------	26
3.19	Effect of tool radius at micron and submicron machining--	28
4.1	Schematic of ESEM chamber------------------------	30
4.2	Schematic of ESEM stage----------------------------	31
4.3	Schematic diagram of first design------------------	34
4.4	Schematic of stage control circuit and force sensing. circuit---	37
4.5	Schematic of second design-------------------------	39
4.6	Schematic of third design--------------------------	41

5.1	SEM micrograph of material flow that occurred when the workpiece was struck by the indenter (Load: 0.035 N and scratching speed: 0.143 mm/sec)--------	45
5.2	SEM micrograph of representative scratched groove surface (Load:0.035 N and Scratching velocity: 0.143 mm/sec)---	45
5.3	SEM micrograph of a smooth groove produced in the *in-situ scratching* mode(Load:0.035 N and scratching speed: 0.143 mm/sec) --------------------	47
5.4	SEM micrograph showing a fractured surface generated at (Load:0.15 N and scratching speed: 0.143 mm/sec)	47
5.5	SEM micrograph at higher magnification view of the crack produced in Figure 5.4 -------------------------	48
5.6	SEM micrograph of a chip measuring approximately 80 μm.(Load:0.15 N and scratching speed: 0.143 mm/sec) --------------------------------------	48
5.7	SEM micrograph showing a ribbon like chip measuring approximately 40 μm long at (Load:0.15 N and scratching speed: 0.143 mm/sec)--------------------	49
5.8	SEM micrograph of twisted chip.(Load:0.15 N and scratching speed: 0.143 mm/sec)--------------------	49
5.9	SEM micrograph of groove formed by 115 ^{o} indenter, (Load:0.035 N and scratching speed: 0.143 mm/sec) smooth grooves without microcracks can be seen ----	50
5.10	SEM micrograph showing higher magnification view of the groove illustrated in Figure 5.9----------------	50
5.11	SEM micrograph showing overall view of groove	

formed due to 0.2 N load and 0.52 mm/sec speed----- 51
5.12 SEM micrograph showing burrs at the edges of the groove formed during scratching --------------------- 51
5.13 SEM micrograph of another kind of chip formed at 0.2 N load and 0.52 mm/sec speed ------------------- 53
5.14 SEM micrograph showing a long chip measuring approximately 30 μm at conditions as in Figure 5.13 --53
5.15 SEM micrograph at higher magnification, showing long chip separated from the side of the edge-------- 54
5.16 SEM micrograph showing smooth groove formed under low load and low velocity scratching with a 75° cone angle indenter -------------------------------- 54
5.17 SEM micrograph of overall view of low velocity and high load scratched surface with a 75o indenter- 55
5.18 SEM micrograph of the chip shown in the Figure 5.17 at high magnification -------------------------------- 55
5.19 SEM micrograph of overall view of groove formed at 0.2 N load and 0.52 mm/sec velocity -------------- 56
5.20 SEM micrograph of chips formed at high load and high velocity -------------------------------------- 56
5.21 An SEM micrograph of chip that appears highly stressed, formed at 0.2 N load------------------------ 57
5.22 SEM micrograph of a brittle chip formed at 0.2 N load- 57
5.23 SEM micrograph of another type of chip ------------- 58
6.1 Tool tip and workpiece at higher magnification ------- 59
A1.1 Schematic of ESEM showing pumping system and electron optics ------------------------------------- 70

A1.2 Schematic showing principle of signal production and collection-- 71
A2.1 Detailed dimensions of table T ----------------------- 72
A2.2 Detailed dimension of tool holder -------------------- 73
A2.3 Front view of third design---------------------------- 74
A2.4 Base plate-- 75
A2.5 Workpiece holder ------------------------------------ 76
A2.6 Ball screw assembly mounting plate ----------------- 77
A2.7 Tool holder.for third design------------------------ 78
A2.8 Piezo mount -- 79
A2.9 Precision ball screw assembly [32]------------------ 80
A2.10 Ultraprecision linear slide [31]----------------------- 81
A2.11 Stacked design of PZT [28]-------------------------- 83
A2.12 PZT outer casing dimensions [28] ------------------- 83
A2.13 Schematic cross section through a three component force measuring element [29]----------------------- 85
A2.14 Graphical representation of range selection [29]------ 87
A2.15 Diagram illustrating the application of force [29]------ 87
A2.16 Diagram of force measuring element [29]------------- 87
A2.17 Workpiece holder speed as a function of applied dc voltage--- 89

CHAPTER I

INTRODUCTION

Glass is a brittle material available in nature. It is an inorganic material supercooled from a liquid state to a rigid condition without crystallization. Glasses are initially ground and then polished to obtain an optical quality surfaces. In polishing, material is removed by loose abrasives, where as in grinding material is removed by a fixed abrasive (grinding wheel). In polishing, the improvement of surface finish is accompanied by a slight deterioration of the contour accuracy of the workpiece. Also, polishing requires more time and is rather difficult to automate [1]. On the contrary, grinding can be automated and contour accuracy can be reasonably maintained. Hence, from the economic standpoint of glass machining, it is advantageous to minimize or eliminate polishing and obtain as good a surface just by grinding. But, the conventional grinding machines cannot produce as good a surface as in polishing. Currently, a new generation of precision machines are evolving to meet this need. These machines are extremely rigid, isolated from external vibrations, and posses features that enable low depths of cut. But, the production of mechanically sound parts from brittle materials, such as glasses and ceramics also depends very much on the understanding of the mechanism of the material removal at low depths of cut.

Brittle materials, such as glasses and ceramics normally respond to applied force during scratching by the generation and propagation of cracks. Figure1.1 is a schematic showing the material removal mechanisms due to brittle fracture proposed by Evans and Marshall [2]. According to this model, above a critical normal load, P_n, stresses in the plastic zone will generate fracture damage in the form of lateral and median crack systems. Below a critical normal load,

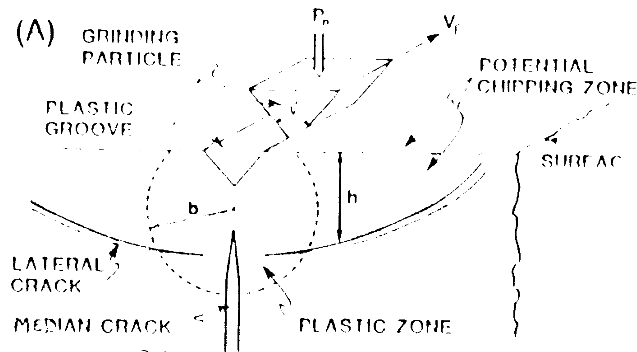

Figure 1.1. Material removal mechanisms due to brittle fracture after Evans and Marshall [2]

microcracks formed may not propagate into bulk material. It is this microcrackfree grinding that is central to precision finishing processes. Much data exist on the fracture of brittle materials and is well understood, but the actual mechanisms that underlie microcrack -free precision finishing technology are not well established at the present time.

Taylor [3], in 1949, was among the first to report on the possibility of formation of microcrackfree grooves on glass by indenting it with diamond pyramid under very light loads (50 gms). Kendall [4], Marsh [5], Ernsberger [6], Blake [7], Puttick [8], and Schinker [9] conducted indentation and scratching experiments on various types of glasses and concluded that producing microcrackfree grooves was possible, but differed on the mechanisms of their formation. Ernsberger [6] and Peter [17] pointed out that it was a densification effect, Taylor [11] and Marsh [20] pointed out that it was plastic flow similar to metals. Both theories have certain drawbacks, because there is evidence for the material removal during ductile groove formation which is against the densification theory and the fact that glass is an amorphous material with no long range order is against the plastic flow concept.

The objective of the current investigation is to design and build an ultraprecision *in-situ* stage for scratching inside an environmental

scanning electron microscope (ESEM), and to study the mechanism of microcrackfree material removal in soda lime silica glass. The scratched samples are also examined inside a conventional SEM for higher resolution.

Chapter II briefly presents the structure of glass, effect of network modifiers on the properties of glass, and machining of glass. Chapter III reviews the literature on scratching experiments. Chapter IV deals with the design of the *in-situ* scratching stage. Chapter V deals with the experimental procedure and test results of the scratching experiments. Discussion is presented in Chapter VI. Chapter VII presents conclusions and Chapter VIII recommend action for future work. Appendices briefly describes the ESEM, lists the technical specifications of various transducers and controllers used in building the current set up, such as piezo electric dynamometer, charge amplifier, piezo actuator, piezo controller, precision ball screw assembly and ultra precision linear slide, and illustrates the detailed drawings of the components used in building the scratching stage.

CHAPTER II

GLASS

Definition and Structure of Glass: Glass is an inorganic material which has been supercooled from a liquid state to a rigid condition without crystallization. At high temperatures, glasses are true liquids but of very high viscosity. The viscosity (10-100 Pa at melting temperature for soda lime silica glass) increases continuously and very rapidly as the temperature decreases (viscosity at room temperature 10^9 Pascals for soda lime silica glass). The rapid increase in viscosity together with rapid cooling as the glass is shaped prevents crystallization.

Structure of Glass: The main types of glasses used commercially are silicate glasses. They are based on a SiO_4 tetrahedra structure, plus some modifying ions.

Silicate Tetrahedral Unit: Here one silicon atom fits between four oxygen atoms. The forces holding these tetrahedra involves both ionic and covalent bonds. Figure 2.1 illustrates the tetrahedral arrangement of SiO_4 .

Structure of Pure Silica Glass: Figure 2.2 shows schematically the structure of pure silica glass. Silicon is at the center of regular tetrahedra and oxygen occupies the four corners. There is no long range order in the glasses. Actually, they are in a state intermediate between a liquid, where no permanent atomic neighbors exist, and a crystalline lattice, where all neighbors are fixed in nearly perfect orderliness .

Network Modifiers: Most silicate glasses contains network modifiers as their presence markedly lowers the high temperature viscosity of glass by reducing the network. This makes glass more

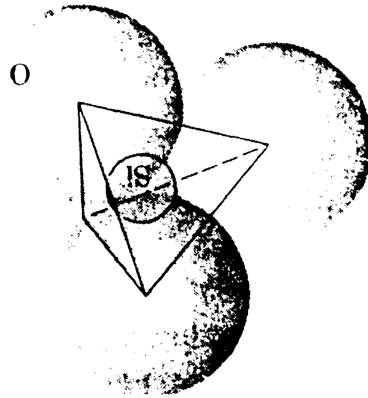

Figure 2.1 Tetrahedral arrangement of SiO4 [11]

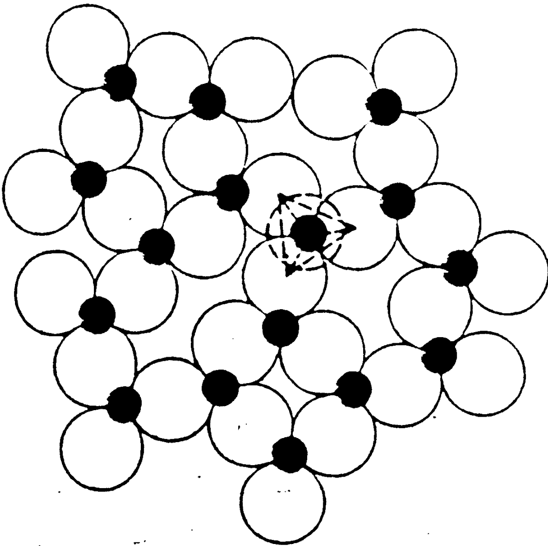

Figure 2.2 Structure of pure silica glass [11]

thermoplastic and much easier to shape into desired products. modifiers are also used to obtain various desired properties, such as corrosion resistance, optical quality, etc. Modifiers are usually oxides,

such CaO and Na_2O. They supply positive ions and nonbridging oxygen ions to the structure of pure silica glass thereby serving the bond at many places. Figure 2.3 illustrates the structure of soda lime silica glass, which is used in the current investigation in the form of microscope slides [12]. Some of the salient properties of the microscope slides glass are presented in Table 2.1 [12]. Soda lime silica glasses costs less, posses good chemical durability, and are available in good dimensional flatness. They are clear and colorless; hence no interference color effects are present during viewing.

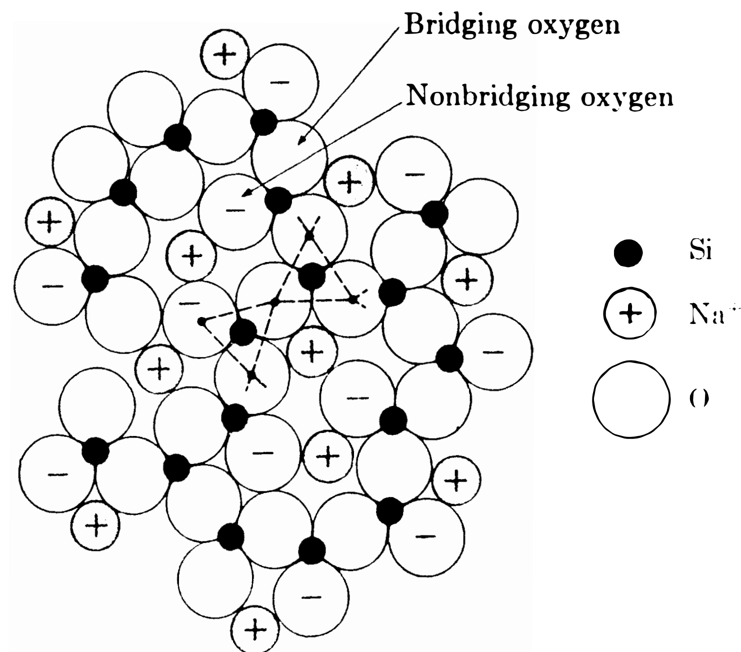

Figure 2.3 Structure of silica glass with network modifiers [12]

Machining of Glass

The material removal in conventional grinding and polishing are somewhat similar, in that, both relay on randomly oriented abrasive particles for the material removal [14]. However, there is a significant difference in the material removal mechanisms in brittle material - brittle fracture and surface damage associated with conventional grinding and microcrackfree surfaces associated with

polishing. This is essentially due to the differences in the depths of material removed and the applied load. This led to the thought that by controlling the infeed rate and load during grinding it would be possible to grind brittle materials without producing microcracks. The material removal at light loads or fine depths of cuts is termed microgrinding [22]. The regime of microgrinding is shown in Figure 2.4 [47]. As pointed out earlier, the possibility of removing brittle materials without producing microcracks was proposed as early as 1949 by Taylor [3]. In chapter III, we shall briefly review the work of various researchers who contributed to the knowledgebase of microcrackfree grinding of glass and other brittle materials. The machining of glasses is described briefly in the following.

Table 2.1 chemical and physical properties of soda lime silica glass

Composition	Si: 71-73 % by weight; Na_2+K_2O: 12-14%; CaO+Mg: 11-16%; Al_2O_3: 0.5-1.5%
Thermal expansion	87 X 10^{-7} / 0 C
Softening point	725 - 735 o C
Density	2.5 gms. per cc.
Refractive index	1.51
Young's modulus	69 Gpa
Strain point	511 o C
Anneal point	545° C
Viscosity at room temp.	10^{9} Pascals
Viscosity at melting temperature	10 - 100 Pascals

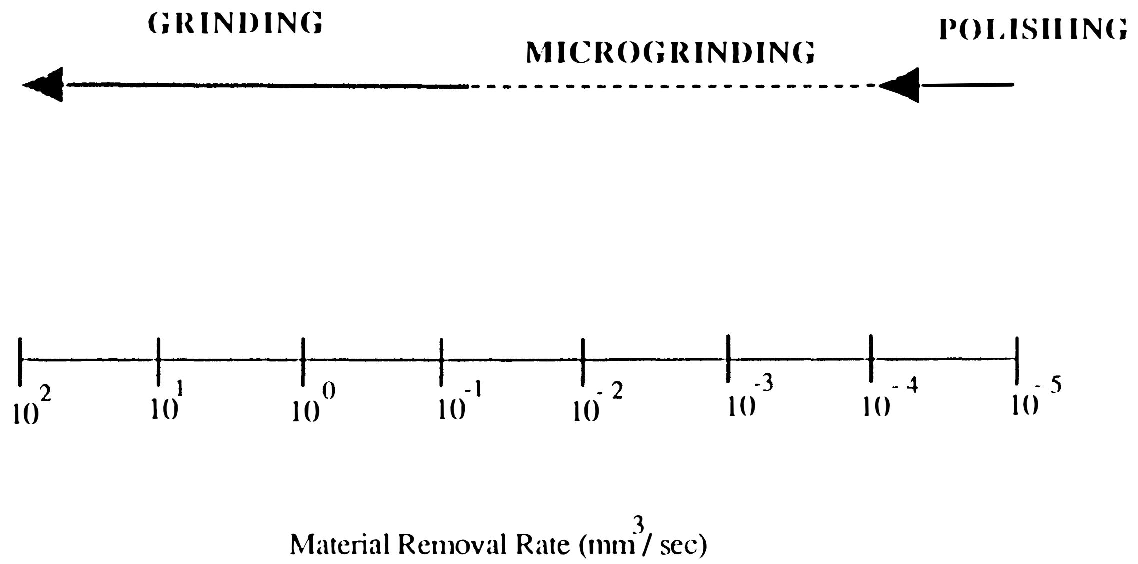

Figure 2.4 Microgrinding regime (after Miyashata [47])

CHAPTER III

LITERATURE REVIEW

Review of Scratching Experiments

In 1949 Taylor [3] found that when glass surfaces were indented with a pyramidal diamond indenter perfect impressions were formed for loads up to 50 gms as illustrated in Figure 3.1. Fracture occured at higher loads. He conducted experiments on over fifteen types of glasses and found similar results. He also, confirmed the same results with low-load scratching experiments. The load and velocity of scratching, however, were not reported. He reported plastic flow in glass and pointed out that its nature was no different than that of metals.

Taylor's findings were received with skeptism as it is difficult to conceive any type of failure other than fracture was unthinkable for a perfect brittle material like glass. But, this led to a plethora of research because of its obvious implications in the strength and reliability of glass finished by this method [6]. Anisworth, in 1954, performed indentation of glass by a diamond pyramidal indenter [15] and supported the view point of Taylor.

Smekal and Madelung initially considered the effect to be one of localized and transient heating, to permit viscous flow. But, later Smekal disregarded this suggestion and proposed that the surface region of glass is normally in a plastic state because of absorption of the ambient moisture.

Marsh [5] reported indentation and scratching studies on soda glass using a diamond indenter. Figure 3.2 shows the indentation impressions formed on steel and glass plates. The smooth grooves he obtained by scratching are shown in Figure 3.3.

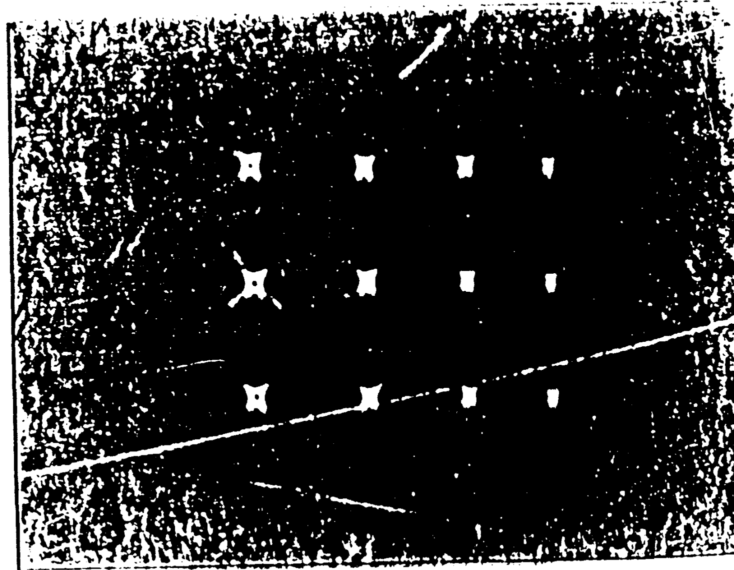

Figure 3.1 Indentations produced on an extradense flint glass (after Taylor [3])

Marsh then presented the following as evidence for plastic flow:

1. The plastic furrows produced by a hard point on a glass surface, as illustrated in Figure3.3.

2. Diamond hardness indentations (Figure 3.2) on soda glass and on steel made by the same indenter. Marsh observed that both are very similar.

3. Residual stresses that were found after the load was removed.

4. High fracture energies of glasses, (which was at least fifty times greater than the surface energy predicted by brittle fracture theory) were found.

5. Failure of glasses to reach the predicted terminal fracture velocities typical of brittle solids.

6. Gross plastic flow found when premature failure is prevented by high the hydrostatic pressures.

Marsh reported that plastic flow in glass is proportional to the network modifiers introduced in the structure, with the hardness

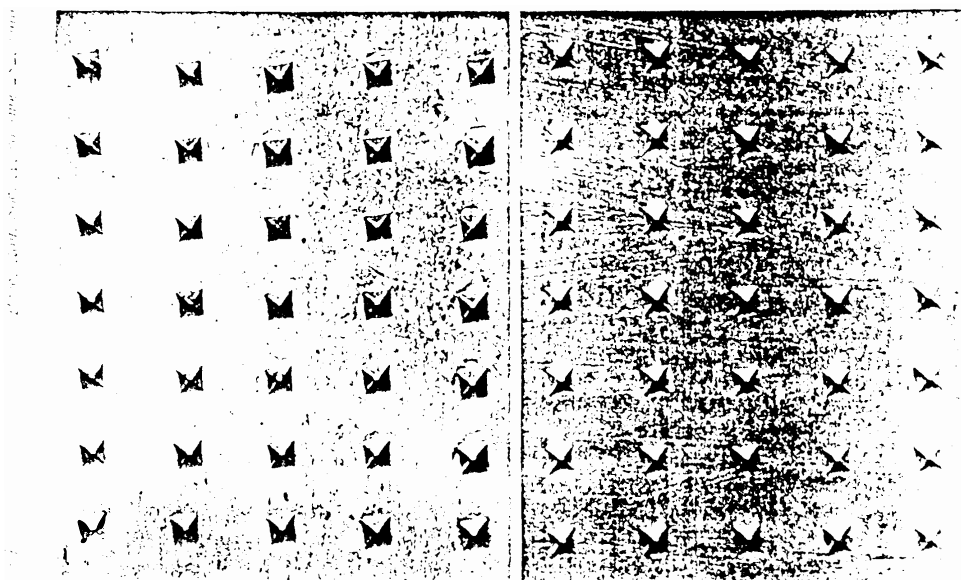

Figure 3.2 Indentations of soda glass and Steel produced by a vickers indenter (after Marsh [5])

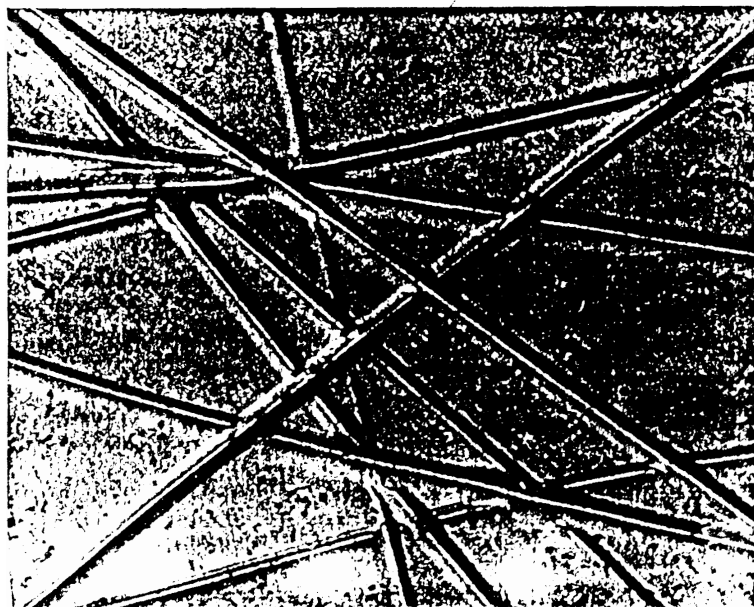

Figure 3.3 Scratches produced by a hard point over glass (after Marsh [5])

falling rapidly as the network modifiers are added. The addition of modifiers creates nonbridging atoms in an otherwise complete network. Hence, he suggested that flow is facilitated by having large

numbers of nonbridging atoms which are loose ends in the network and permit flow in a manner somewhat analogous to the half planes which terminate at dislocations in crystals.

But, Ernsberger [6], interpreted this as not plastic flow but due to densification effect, because of the fact that densification occurs strictly under hydrostatic conditions. This suggests that mechanism involves a simple collapse of the structure into a more closely packed arrangement involving minor bond rotations and changes in the bond angles. Ernsberger devised an interferometric technique and illustrated that the refractive index of the silicate glasses increased at the point directly below the indenter by 8%. It is known by the Lorentz theoretical equation that density is proportional to the refractive index. He estimated that the minimum depth of the densified zone is about one fourth the indenter diameter.

Peter [16], also, conducted indentation studies and reported the effect of densification. He pointed out that densification is due to movement of a group of atoms with the atoms strongly bound to each other within the group but loosely bound to the surroundings, with the exception of one atom. At this site, a local stress concentration is generated providing energy for the motion. He showed the local increase in the refractive index by optical observations, as shown in Figure 3.4.

Hureata and Malkin [17] pointed out that the material removal mechanism is different when grinding glass with silicon carbide abrasive than with diamond. They proposed that material removal in glass with silicon carbide abrasive occur by viscous flow into chips but material removal with diamond occurs by brittle fracture, which is preceded by viscous deformation on a small scale. The specific grinding energies with diamond are an order of magnitude less than with silicon carbide (as illustrated in Figure 3.5) since a much smaller volume of material undergoes viscous deformation. They pointed out that temperatures generated during grinding plays a key role in determining the mechanics of material removal. They reported that the surface temperature generated when grinding with silicon

carbide grinding wheel was above the glass transition [Tg] temperature. But, due to much lower energies for the diamond grinding, the average surface temperature reaches only about 15% of the glass softening temperature. Hence, they reasoned that gross viscous flow should not occur over the grinding zone with diamond abrasives.

Golini and Jacobs [18] proposed a mechanism of material removal in loose abrasive microgrinding, as illustrated in Figures 3.6 (a), (b) and

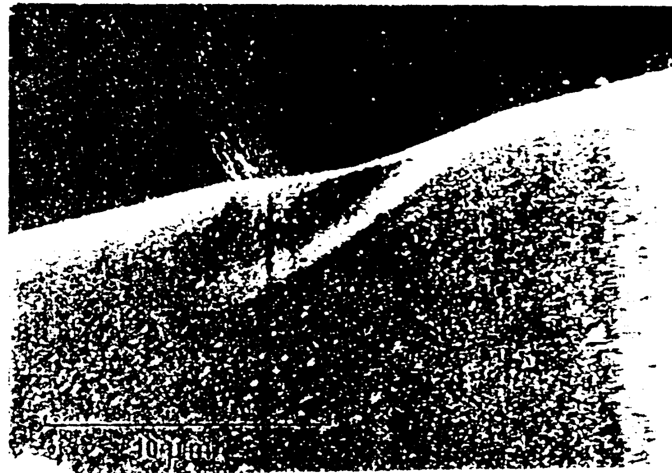

Figure 3.4 Profile of ball indentation on plate glass (aftrer Peter [16])

(c). They argued that a brittle mode ground surface consists of a disrupted uppermost layer and a subsurface compacted layer. Brittle fracture occurs because of microindentations produced in the microgrinding process. Subsurface damage extends into the bulk material with a magnitude nearly equals the abrasive size. A ductile mode of loose abrasive ground surface consists of an uppermost compacted layer lying above the bulk material. Little subsurface damage is produced by this process. The ductile surface is the result of glass removal due to shearing, where the glass is actually planed off on a microscale, and the magnitude and depth of deformation are dependent on the abrasive size. They also reported a third mode of grinding where little glass is actually removed but smeared from the peaks to the valleys.

Kendal [4] pointed out that plastic deformation, being essentially a volume process, depends upon the cube of the characteristic dimension. On the other hand, crack generation and crack propagation are proportional to the area of the crack i.e. the square of the characteristic dimension. As the characteristic dimension gets smaller, the amount of energy necessary to initiate plastic deformation becomes lesser than that required for crack generation. It, therefore, follows that at a certain critical depth, the plastic deformation process is energetically favoured compared to the crack

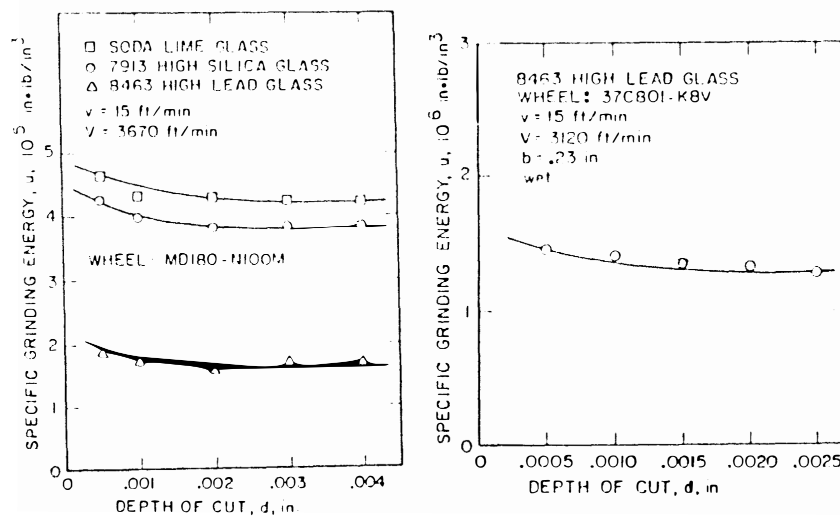

Figure 3.5 Specific grinding energies during grinding with diamond and silicon carbide [17]

generation process. The model developed by Kendall predicts that crack propagation cannot occur in particles of dimension smaller than

$$d_c = \frac{10\ E\gamma}{\sigma^2}$$

where γ is the fracture surface energy, E is the youngs modulus and σ is the yield stress.

Now, as it appears feasible that grinding of brittle materials can be accomplished without producing largescale microcracks, attention was focused by many researchers [7-9, 20] on, the critical depth of

cut, minimum load, grinding velocity, types of abrasive, its grain size, etc. of the microcrackfree grinding as of these parameters have practical implications on the microcrackfree grinding of brittle materials.

King et al [19] in 1954, reported about the possibility of grinding brittle materials in the ductile regime. Based on an experimental study of crystalline materials (rock salt, lead sulfide and ice) King reported that under high hydrostatic pressures in brittle materials, fracture is prevented and a marked plastic deformation process steps in. Under these conditions, plastic yield stress reaches values very much greater than the bulk shear strength of the undeformed specimen. This essentially brittle to ductile transition is attributed to "healing" of the flaws and the consequent inhibition of brittle fracture.

Swain in 1979 reported that material removal progressed in three stages, namely, plastic grooving, generation of lateral and median cracks, and crushing. He reported that the sequence is directly related to the force on the abrasive grain, with lower forces corresponding to an increase in grinding ductility.

Hagan [21] conducted indentation experiments on soda-lime silica glass and proposed a model for obtaining the minimum load for crack nucleation. According to the model, the minimum load for crack nucleation depends on the hardness, H and the critical stress intensity factor, K_{IC}.

$$P_c = \frac{K_{IC}}{H} \times K_{IC} \times 885$$

$$K_{Ic}^2 = \frac{E\,\xi}{1 - \nu^2}$$

Where ν is the poisson's ratio and ξ is the strain energy release rate which is approximately twice the fracture surface energy. Hagan found that the critical normal load for crack nucleation to be 0.008 N for soda-lime silica glass.

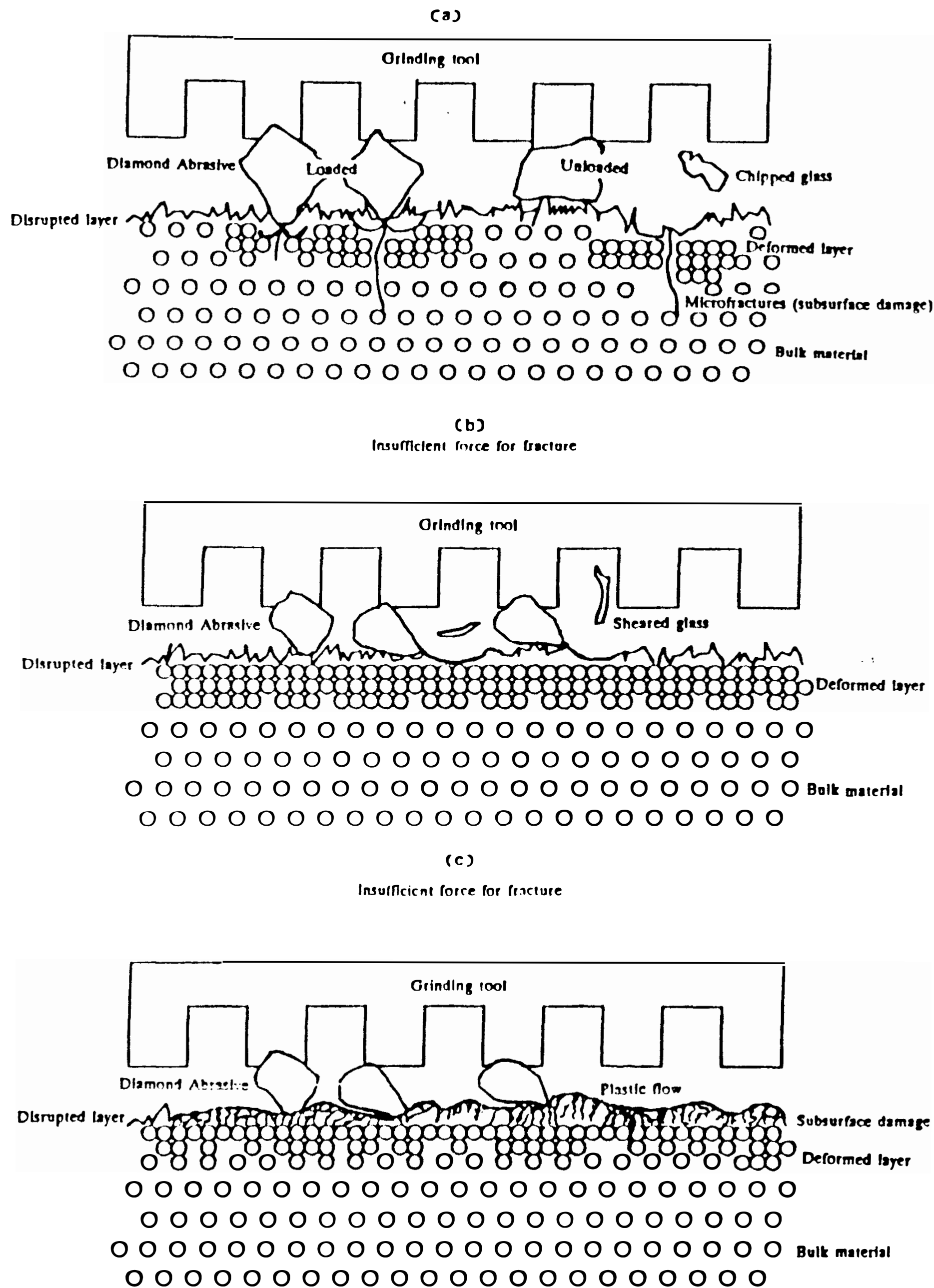

Figure 3.6 Proposed model for loose abrasive microgrinding (a)brittle (b) ductile and (c) glass flow (after Goloni and Jacobs [18])

Grenou and Veldkamp [20] conducted scratching experiments on different brittle materials including zink oxide, lead glass, Sr hexa ferrite, manganese zink ferrite, nicklezink ferrite and aluminium oxide. The apparatus used is shown in the Figure 3.7. A diamond ground to the shape of a square base pyramid constitutes the scratching tool. They conducted scratching experiments with scratching velocities ranging from of 0.4 μm/sec to 400 μm/sec and normal loads ranging from 0.05 to 0.5 N. Figure 3.8 shows the

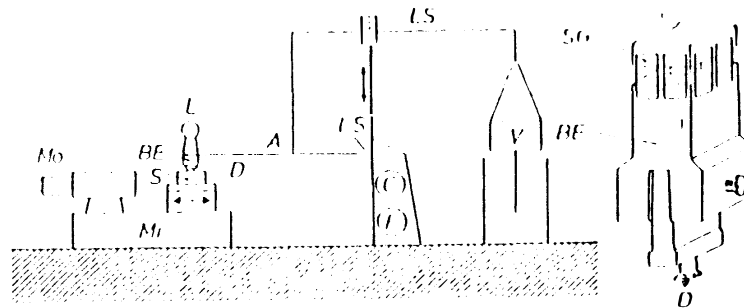

Figure 3.7 Scratching apparatus developed by Van Groenou and Veldkamp [20] S - Sample Mo - Motor, Mi - Micromanipulator, A - Arm, L - Load, C&F - coarse & fine vertical adjustment, V - Counter weight, S - Damper, BE - Bending element, SG - Strain gauges.

surface variation (Fn) with cutting velocity. They divided plot into three regions by boundaries I and II. Region A is designated as the region of formation of clean grooves, B the region of cracking, and C the region of cracking and chipping.

Schinker [9] performed scratching experiments with a single point diamond tool using the set up illustrated in Figure 3.9. He claimed that his set up had avoided bearing play, vibrations, and thermal drift which are necessary to machine brittle materials without producing microcracks. He reported scratching of various glasses, including BK-7, soda lime glass, SF 5, SF 6, 900, 403, 554 and 666 at scratching speeds ranging from 1 μm/sec to 100 m/sec and depths of cut upto 15 μm. He examined the scratches using polarized, interference, and dark field microscopic techniques. He pointed out that plastic groove is a parameter of critical depth of cut which varied from 0.3 μm to 2 μm depending upon the scratching speed,

($V_{critical}$) and the type of glass. He observed large scale lateral cracks and median cracks below the critical scratch speed. This was reported to be ≈ 20 m/sec, depending on the type of glass used. At low scratching speeds, he showed that traces of slip faces are induced by shear under high indentation pressures. Besides plastic deformation, highly densified or compacted glass was produced at the bottom of the groove. Also, median cracks and large scale lateral cracks were observed, due to residual stresses induced after the

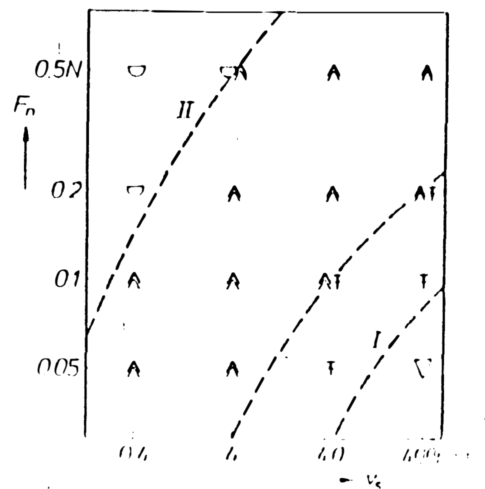

Figure 3.8 Surface variation as a parameter of applied load and scratching velocity (after Goneru and Veldkamp [20])

removal of the diamond indenter. He reported that with an increase in scratching speed to $V_{critical}$ (which depend on the type of glass used) drastic changes in deformation the behavior was observed, i.e., from a highly viscous flow to low viscous flow, induced by a temperature rise in the deformation zone. No evidence of median and large scale lateral cracks was found, but conchoidal cracks were detected at deeper scratches. Figure 3.10 illustrates extremely thin, long chips obtained by Schinker at 100 m/sec scratching speed on a RS 520 glass surface.

Puttick [8] proposed that transition from a brittle to a ductile failure occurs when a certain length attains a critical value. He proposed a model for the critical depth of cut. Considering the strain energy 'Λ' Contained in a strained volume of length 'a', width 'w' and depth 'B'.

$$\Lambda = \frac{\sigma_r^2 \ w \ a \ B}{2 \ E}$$

where σ_r is the compressive stress and $A \approx w\,a$ is the contact area

$$\frac{d\Lambda}{dA} = \frac{\sigma_r^2 \ B}{2 \ E}$$

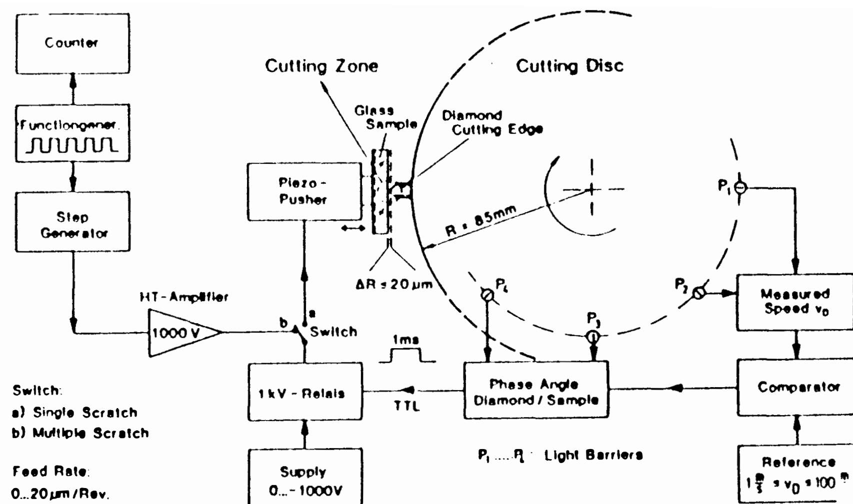

Figure 3.9. Schematic diagram of the scratching setup (after Schinker [9])

For delamination under shear

$$\frac{d\Lambda}{dA} = R_{11}$$

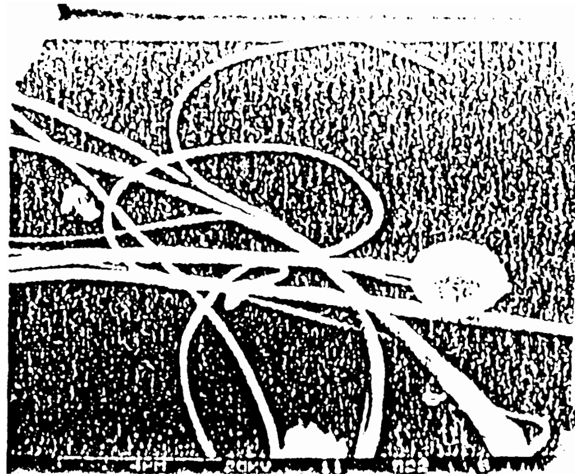

Figure 3.10 Long , thin chips.reported at a scratching speed of 100 m/sec (after Schinker [9])

where R_{11} is the fracture toughness in shear.

Hence, the critical depth, Bc is given by

$$B_c = \frac{2 E R_{11}}{\sigma_r^2}$$

Puttick's apparatus is shown in Figure 3.11. The glass sample was mounted on the spindle and rotated at low speed (6 rpm) and the depth of cut was given through a piezo actuator. He reported generation of crack free surfaces and chips at lower speeds. Figure 3.12 illustrates the swarf produced in low speed scratching of Spectrosil. Puttick [8] suggested that grooves were formed by a combination of elastic-plastic deformation and a ploughing process. His findings, however, contradicts that of Schinker's [9] because he imposes a critical scratching speed below which a crack free surface cannot be obtained. Puttick did point out that speed has an effect on the ductile machining of glass. He reported that increasing the speed, the critical depth of cut can be increased.

Blake and Scatterwood [7] used a parallel axis ultraprecision lathe (PAUL) as illustrated in Figure 3.13. They reported a surface finish R_a of 0.8 nm on a germanium disk and proposed a mechanism for microcrackfree machining as illustrated in Figure 3.14. They pointed out that the so called ductile regime machining is by no means a regime wherein material is removed in a ductile fashion. Material removal in the uncut shoulder above the critical chip thickness t_c in Figure 3.14 occurs by a combination of plastic flow and extensive microfracture. For effective chip thickness $t_{eff} > t_c$, a microfracture damage zone is formed along the tool nose. Ductile cutting without fracture occurs only along the lower portion of the chip cross section

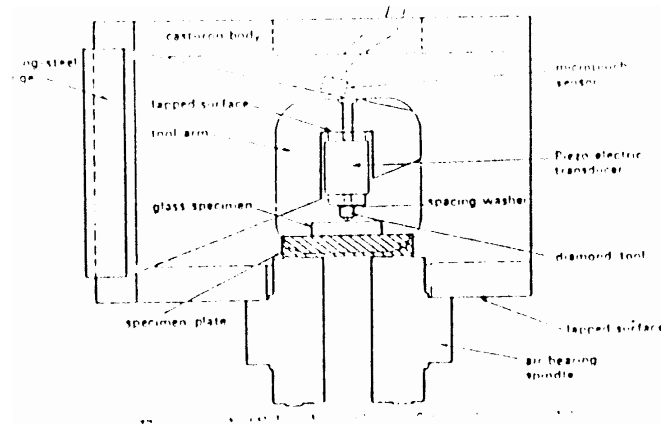

Figure 3.11 Schematic diagram of the scratching set up (after Puttick [8])

where $t_{eff} < t_c$. The material could still be machined without surface damage if the microcracks generated did not penetrate the plane of the cut surface. They reported that tool rake angle and tool clearance angle have considerable influence on the critical chip thickness and the cutting speed has negligible effect on the critical chip thickness. These are illustrated in Figures 3.15 and 3.16 and Tables 3.1 and 3.2.

Bifano.[22] reported the use of a precision engineering grinding apparatus for super finishing ultrahard surfaces (PEGASUS), in microcrack free regime, as illustrated in Figure 3.17. The rotary [7] motion of the grinding wheel is accomplished by an air bearing spindle which allows grinding speeds up to 5000 rpm with axial error < 40 nm and the grinding infeed is accomplished by a piezoactuator. He came up with a plot (Figure 3.18), of brittle to ductile transition as a function of grinding infeed rate. He proposed that all materials undergo a transition from brittle to ductile machining regime if the grinding infeed rate is made small enough. Below this threshold depth of cut the energy required to propagate cracks is larger than that for plastic yielding. Bifano proposed a model for critical depth as illustrated in the following:

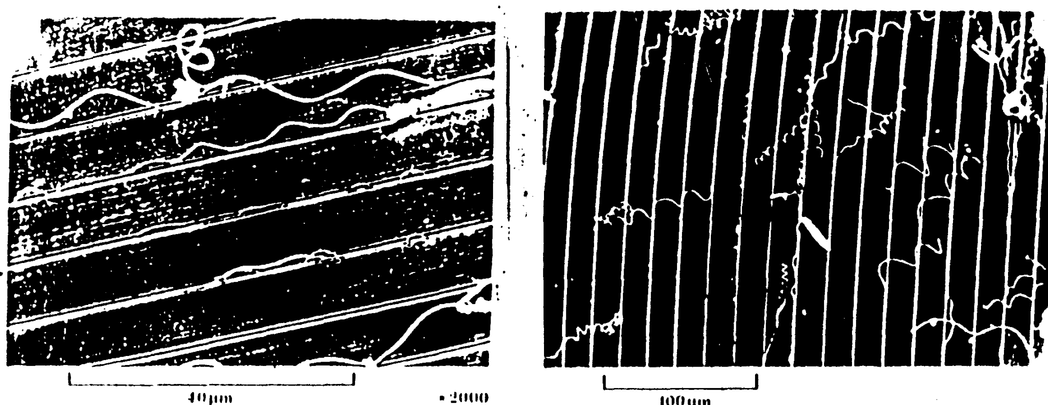

Figure 3.12 Spiral swarf adhering to machined grooves in spectrosil (after Puttick [8])

Considering the elastic strain energy available in the plastic indentation zone of an individual abrasive grain:

$$E_s \, \alpha \left(\frac{H^2}{E}\right) d^3$$

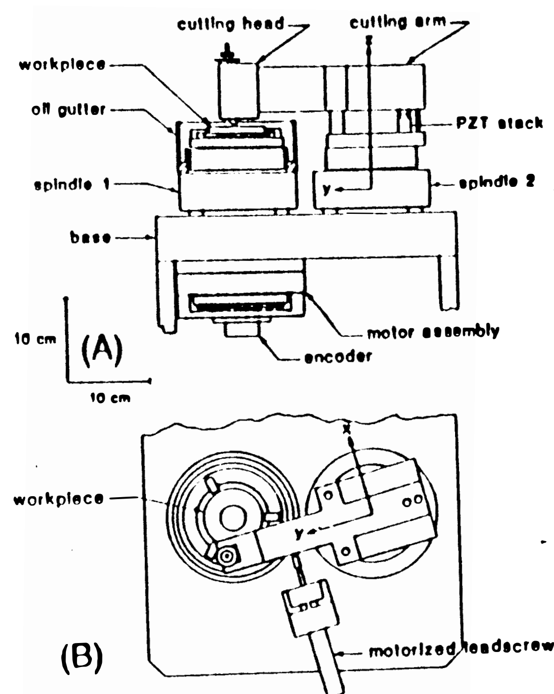

Figure 3.13 Parallel axis ultra precision lathe machine after Blake (and Scatterwood [7])

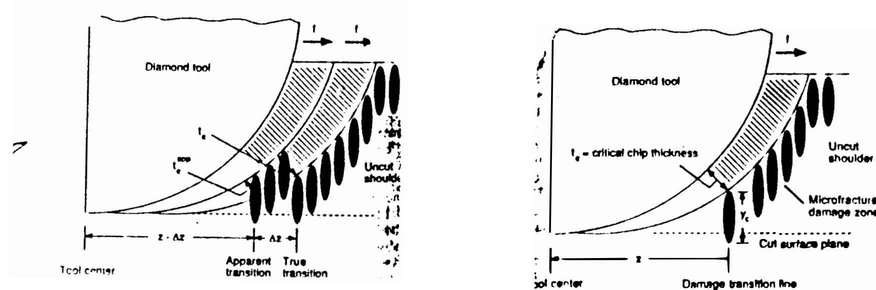

Figure 3.14 Mechanism for microcrackfree machining (after Blake and Scatterwood)

where H is the hardness and E is Youngs modulus. The energy required for the crack formation in the deformation zone is given by

$$E_f \ \alpha \ \gamma \, d^2 \ \alpha \ \left(\frac{K_c}{E}\right) d^2$$

Where Kc is the fracture toughness.

But $K_c = \sqrt{2 \gamma E}$

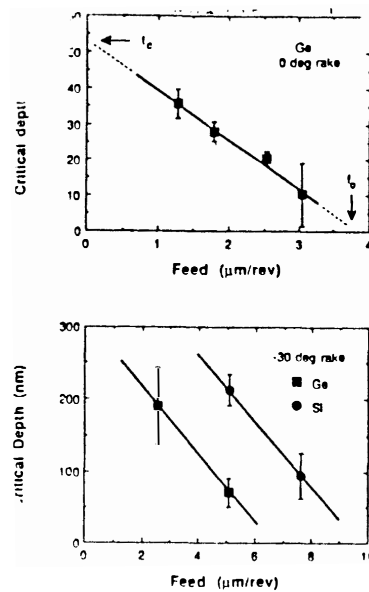

Figure 3.15 Effect of tool rake angle on critical depth [7]

Table 3.1 Effect of tool rake angle on critical depth (after Blake and Scatterwood [7])

Rake angle (deg)	t_c^{crit} (nm)
0	20 ± 2
−10	13 ± 6
−30	165 ± 46

*(100) germanium, f = 2.5 µm/rev, clearance = 6°, speed = 2.1 m/s (95% confidence interval shown for mean values).

Table 3.2 Effect of surface cutting speed on critical depth (after Blake and Scatterwood [7])

Cutting speed (m/s)	t_c^{crit} (nm)
8.2	168
2.1	206
0.84	183

*(100) silicon, f = 5 µm/rev, rake = −30°, clearance = 6°.

Hence, $E_f \ \alpha \ \left(\frac{K_c^2}{2\ E}\right) \ d^2$

and $d = d_{critical} \ \alpha \ \left(\frac{K_c}{H}\right)^2$

He reported that specific grinding energy will remain largely constant for ductile regime grinding but will decrease with an

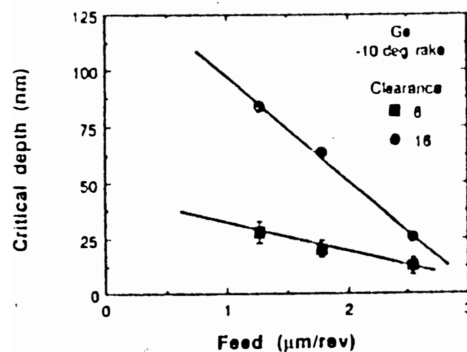

Figure 3.16. Effect of tool clearance angle on critical depth after Blake and Scatterwood [7]

increase in material removal rate [23]. He suggested that the regime of a grinding process can be controlled by monitoring the specific grinding energy in real time. Bifano and Yi [24] further suggested that the ductile regime grinding can be controlled by monitoring the acoustical emission during the grinding process.

Komanduri [25] proposed that depth of cut may not solely dictate plasticity or brittleness of a material, because in order for a brittle material to exhibit plasticity the state of stress should be such that there is a significant hydrostatic pressure of the order of 10Mpa, as reported by Bridgman [26]. Mere changing of depth of cut would not result in change of mode of deformation because it shows result in geometrically similar stresses. This implies that merely changing the depth of cut cannot result in significant increase in hydrostatic pressure or induce ductility at the point of deformation. He, advanced one plausible reason for the existence of a ductile region in grinding at low depths of cut, based on high negative rake angle of

the abrasives present at small depths of cut. In the case of conventional cutting, the edge radius is small compared to the depth of cut. In this case, the rake angle would be determined by the rake face. As the depth of cut becomes small (almost that of the edge radius), it becomes necessary to consider the geometry of the edge radius. At these depths, the edge radius would dictate the rake angle, which will be highly negative, as illustrated in Figure 3.19. As, the rake at smaller depths of cut can be negative, the state of stress can change in such a way that the hydrostatic component may reach high values which can cause plastic deformation.

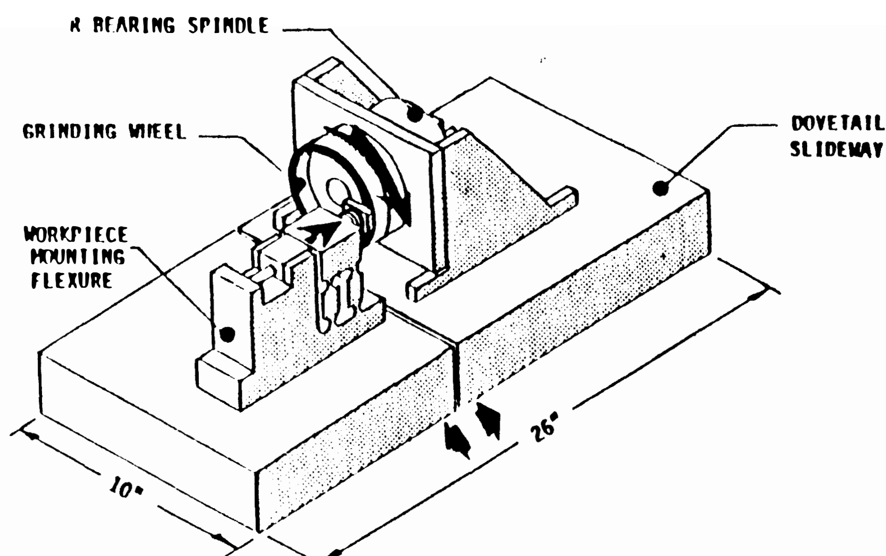

Figure 3.17 Schematic of grinding apparatus (after Bifano [22])

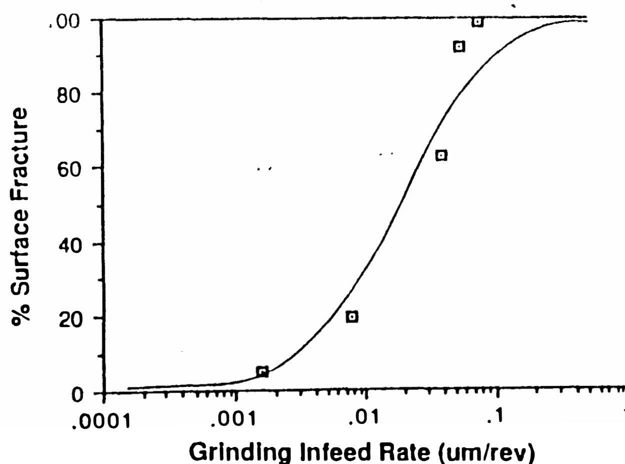

Figure 3.18. Brittle ductile transition as a function of grinding infeed rate for fused silica (after Bifano [22])

According to him, the fact that a machined (or ground surface) is smooth does not necessarily mean that the surface is generated by plastic deformation. For example in diamond, smooth surfaces are produced by cleavage and not by plastic deformation. Temperature effects also play an important role. In the case of glass, as the temperature increases above the glass transition temperature, it becomes viscoplastic, which when machined can produce continuous chips like the ones produced in ductile materials.

From the above review, it appears that grooves can be generated without producing microcracks when a highly brittle material such as glass is indented or scratched under light loads [3-9, 16, 20, and 27]. One school of thought proposed that it is pure plastic flow, as in the case of metals. Another group of researchers suggested it to be due to a pure densification (without any material removal). A third group of researchers proposed that groove formation was due to viscoplastic flow because of the flash temperatures produced during scratching. It is however very difficult to visualize plastic flow in amorphous materials because plastic flow is characterized by dislocation motion on slip planes, which is not possible in amorphous materials. It is also difficult to accept the pure densification theory, because material removal has been reported when scratching glass and other brittle materials. Some researchers reported the formation of chips when scratching glass at low loads. It is therefore important to know the mechanisms of chip formation in scratching glass.

Towards this goal it was decided to design and build an *in-situ* scratching stage for use inside an environmental scanning electron microscope (ESEM). This should enable scratching of brittle materials such as glass, *in-situ*. It was also decided to observe the scratches inside a conventional SEM for higher resolutions.

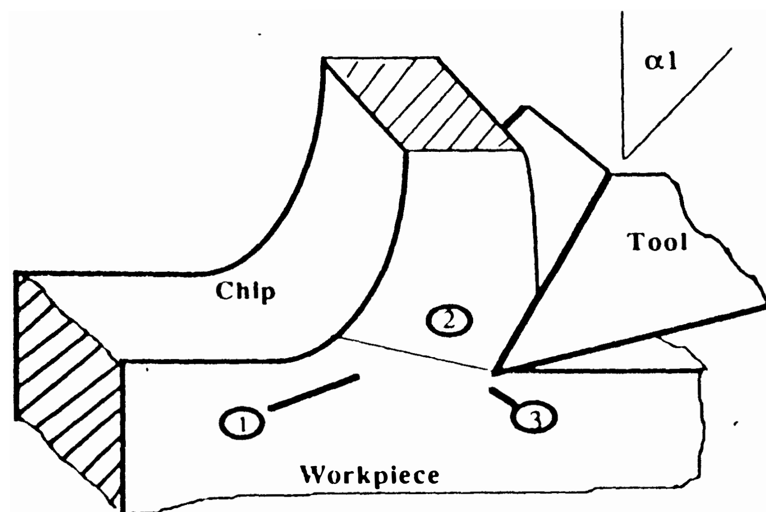

A

1. Primary Deformation Zone
2. Secondary Deformation Zone
3. Teritiary Deformation Zone

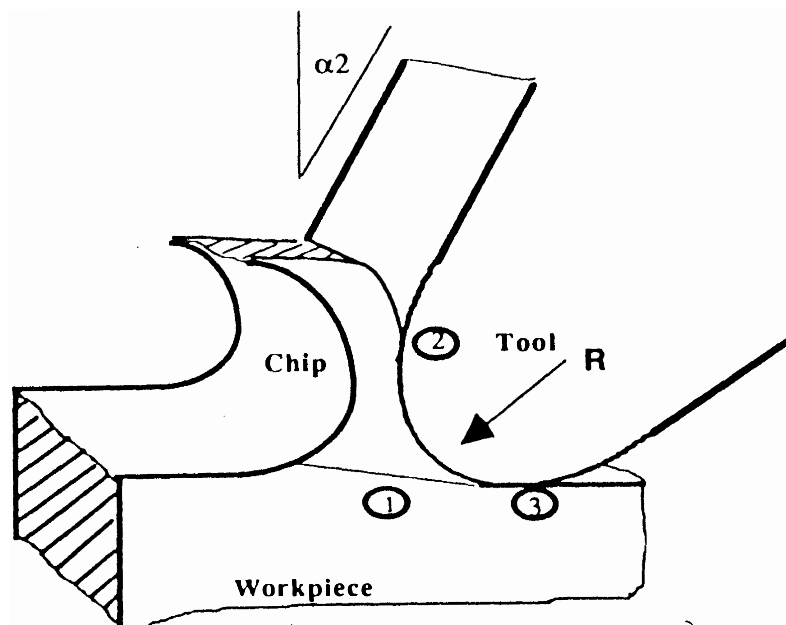

B

Effect of tool radius at submicron machining

Figure 3.19 Effect of tool radius in conventional and submicron machining [19]

CHAPTER IV

DESIGN AND FABRICATION OF *IN-SITU* SCRATCHING STAGE INSIDE ESEM

The environmental scanning electron microscope is similar to a conventional scanning electron microscope in function, but has an additional feature of being able to view nonconducting samples without the need for a conductive coating. Hence, this equipment is ideal for conducting *in-situ* scratching experiments on glass, which is a nonconductor. Appendix A1 is a brief description of the ESEM.

Considerations for the Design of the *In-situ* Scratching Stage for Scratching Inside ESEM

As the scratching apparatus has to be operated inside the ESEM, there are several considerations that should br taken into account for design of the apparatus. The following are some of the important considerations.

1. Figure 4.1 is a schematic of the ESEM chamber with it's main dimensions in inches. The chamber is cylindrical in shape with an internal diameter of 13.5 in and an opening for the door measuring 6.75 in X 11.in The detector, D is situated at the center and on top of the chamber as shown in Figure 4.1. The stage, with X-, Y-, and Z- motions along with their driving motors, is mounted on the door of the chamber as illustrated in Figure 4.2. The gap between the door opening and the top of the stage is 3 in. Hence, the setup designed to perform *in-situ* scratching must be capable of passing through a 6.75 in X 3 in opening, imposing restrictions on the dimensions of the scratching apparatus and force sensing setup.

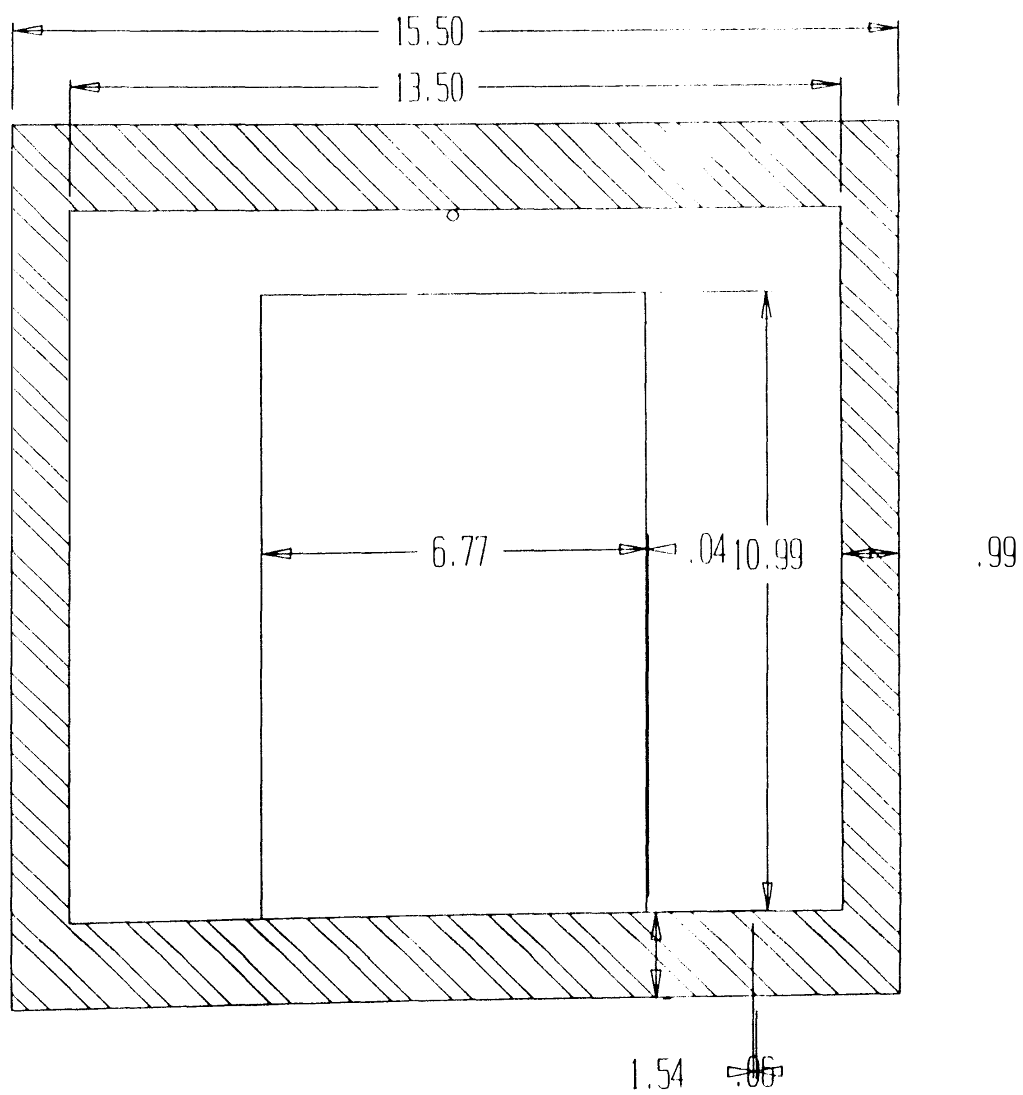

Figure 4.1. Schematic of the ESEM chamber

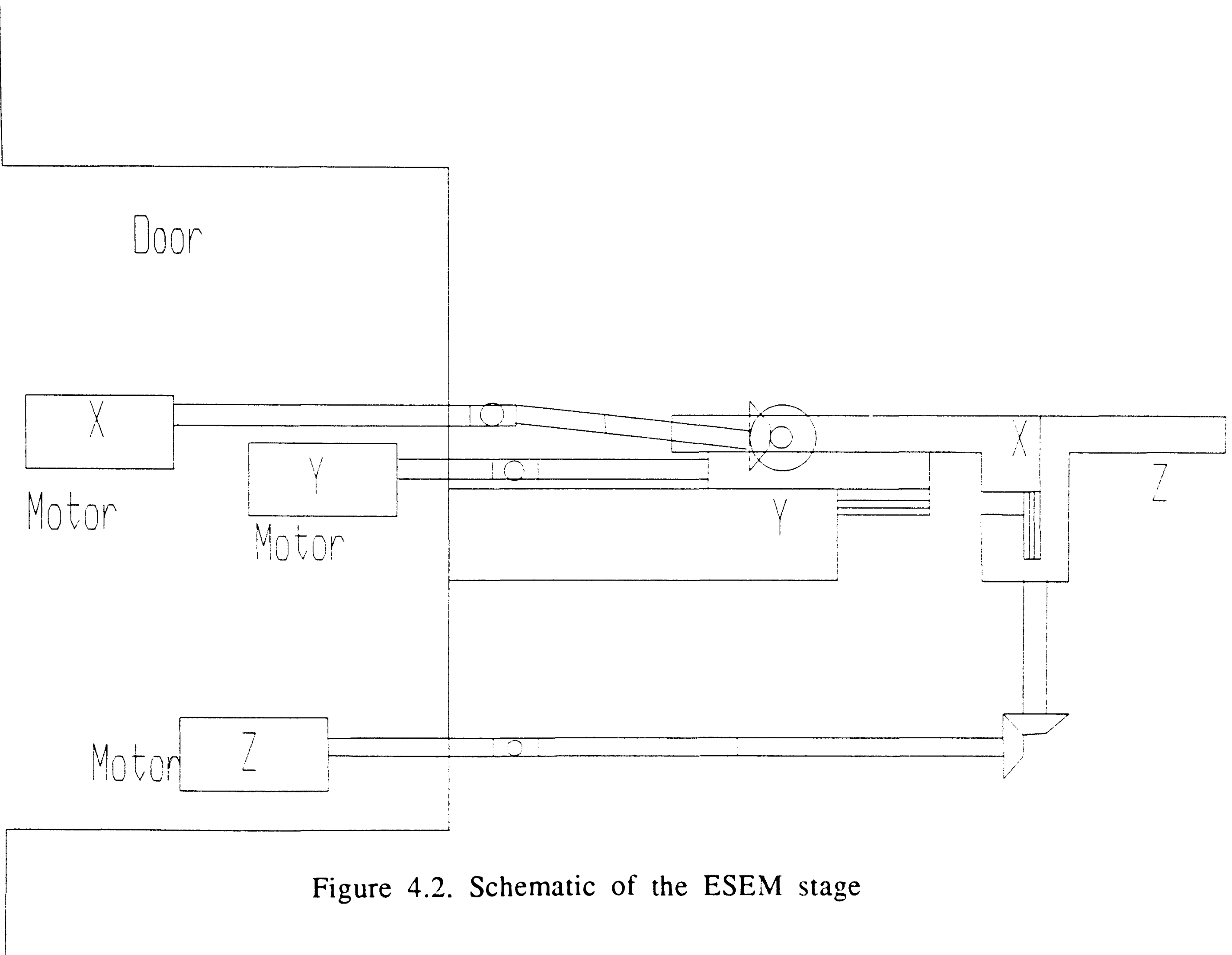

Figure 4.2. Schematic of the ESEM stage

2. X-, Y-, and Z- axes traces a series of motions when the ESEM is switched on, switched off, and calibrated. When the ESEM is switched off, the stage takes a position in a way that it can pass through the chamber opening without colliding with the chamber wall. Similarly, when it is switched on it moves into a preprogramed position near the detector. When calibrated, it traces a preprogramed path and the center of the stage comes directly under the beam. Further, some accessories, such as X-ray analyzer shaft and microinjector shaft are present in the chamber. These further limit the size of the scratching stage. Hence, the equipment should be designed so that it does not strike the X-ray analyzer and microinjector shaft when performing these complex motions.

3. The maximum distance that can be traversed by X-, Y-, and Z- axes are 1.84 in, 1.84 in and 0.894 in respectively. The total weight of the whole apparatus should be less than 7 lb because that is the design load permitted considering the capacity of the stage.

4. Scratching can be done only at slow speeds (less than 0.04 in/sec) in order to video tape the scratching process. If scratching is done at higher speeds, the image has to be viewed at high scan rates which produces low quality image.

5. The tool must be positioned below the detector without vibrations during the cutting process to enable clean viewing of the scratching process.

6. The setup should not produce any stray magnetic fields that can effect the magnetic lenses in the column. Any stray magnetic fields should be properly shielded.

7. The scratching action must take place 0.15 to 0.25 in from the detector to obtain maximum signals, and thus provide a good image.

8. The workpiece should not be tilted more than 45°.

Requirements of the Scratching Apparatus

The major requirements for the scratching apparatus are that it should be compact, vibration free, rigid, and of high precision. Means should be provided for reciprocating the workpiece in order to provide the scratching motion relative to a stationary tool. Means must also be provided for setting up the depths of cut (upto 15 μm) and a force sensing circuit capable of sensing very small dynamic loads accurately.

Taking into account the constraints imposed by the ESEM and the requirements demanded by the microcrackfree scratching process, several designs for the apparatus were attempted, starting with the simplest system requiring minimal additions and modification to the ESEM.

First Design

The ESEM chamber has a shaft S (microinjector shaft) illustrated in Figure 4.3 which is mounted on the chamber wall about 1 in below the top of the chamber, and has two knobs, K1 and K2. The shaft S which can be moved in and out up to 2 in by operating K1 and can be tilted down by maximum of 1 in from its horizontal position in the Z-plane by operating K2. The shaft is about 0.3 in in diameter, and projects approximately 1 in inside the chamber and has a small circular hole on it to facilitate clamping. A rectangular aluminium piece, (11 in. wide, 0.5 in high and 0.5 in thick is mounted and clamped to the shaft as illustrated in Figure 4.3 Another aluminium piece 0.5 in wide, 1 in high and 0.2 in thick) is bolted on to the free end of the aluminium piece, which acts as a tool holder. A diamond tip, with a cylindrical aluminum shank is force fitted into the tool

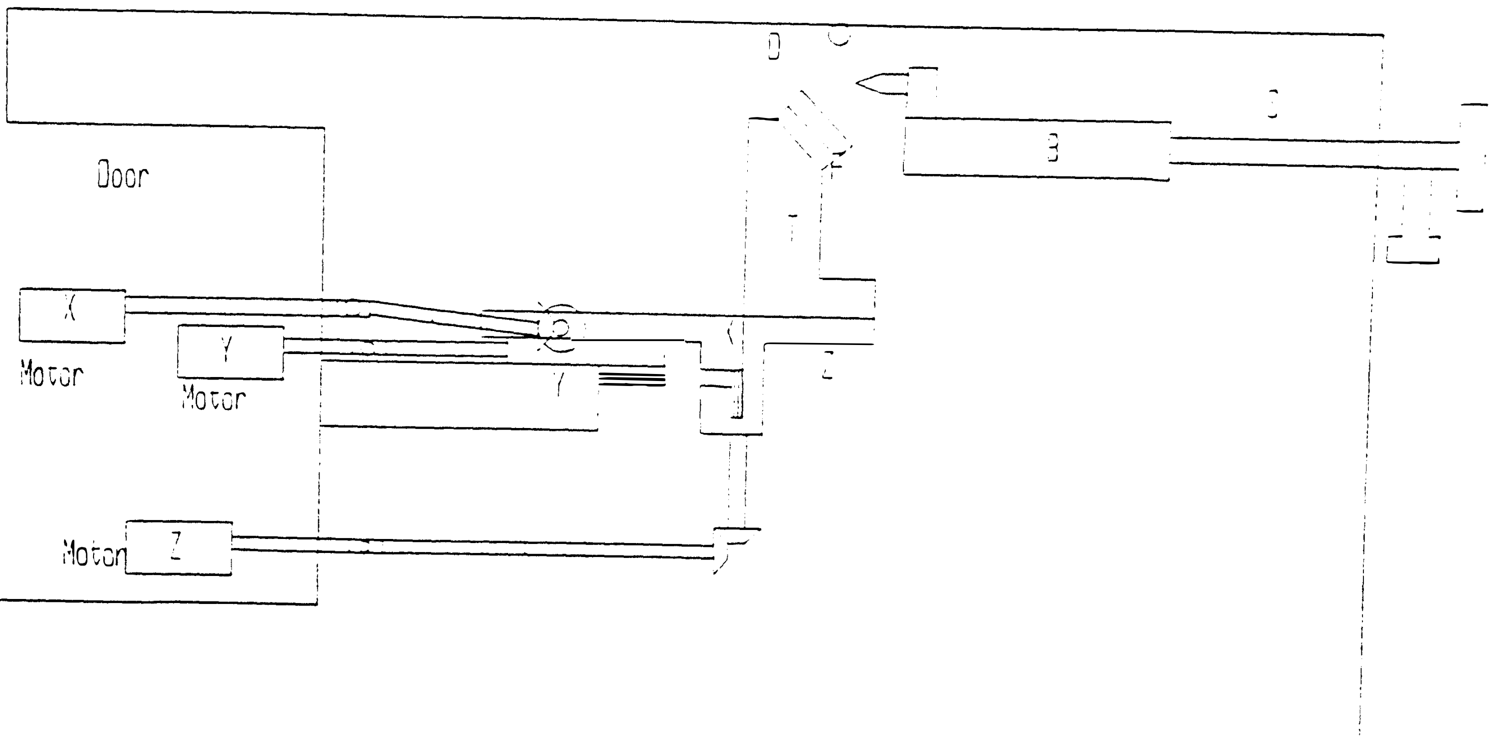

Figure 4.3. Schematic diagram of first design

holder. The scratching tool can now be brought below the beam by operating the K1 and K2. Table T is mounted on the X-, Y-, Z- stage of the ESEM on which the workpiece (glass slide) and the force transducer are mounted. The workpiece is glued on to workpiece holder which in turn is bolted on to the Table T (for details see Appendix A2, Figure A.2.1). The workpiece is positioned by moving the three axes of the ESEM stage. After the workpiece is positioned, movement of the X-axis provides the depth of cut and movement of the Y-axis provides the scratching motion. The tool is held stationary below the detector. The three axes can be controlled by the joy stick or by the software. In the software control mode, every click of the mouse will advance the selected axis by 1 μm, which means it is not possible to obtain the required continuous scratching motion if this option is used. In the joy stick control option, even though we get a continuous motion, we cannot be sure that we are maintaining the same velocity throughout the cut. Furthermore, the stage velocity is a function of the magnification, which means there is no independence for selecting the required velocity. Therefore, one cannot be sure that scratching is done at constant velocity. The ESEM has an accessory, namely CPU transition module to which an RS 232 and a VT 100 could be hooked up to acquire external control of the stage. The control diagram for the stage is given in Figure 4.4. With this, it is possible to access the ESEM software and give the required motion commands and obtain continuous motion of the stage at desired velocities and magnifications.

Force Measuring Circuit

Figure 4.4 is a schematic of the force measuring circuit. A 3-component Kistler piezoelectric dynamometer is clamped by the preloading nut and bolt between the workpiece holder and the table T. The output from the dynamometer is connected to the input of a charge amplifier and the output from the charge amplifier is connected to a digital multimeter. The applied load in all three axes

is read in terms of voltage by three separate digital multimeters. The technical details of the dynamometer and the charge amplifier are given in the appendix A2.

Although the scratching stage appears to have met all the above mentioned requirements, when scratching experiments were conducted it was found that tool was not sufficiently stiff and would deflect thereby removing it out from the field of view. It was also not possible to conduct low load scratching experiments with this setup for the same reason.

Hence, it was decided to retain the same design for workpiece motion control and force measurement but change the way the scratching tool was mounted inside the chamber. This led to the second design.

Second Design

Figure 4.5 is the schematic of the second design and Figure A2.2 gives the detailed drawing of the tool holder for this design. The tool holder is clamped to the stationary part of the stage, as illustrated in Figure 4.5. A stainless steel tube is bolted on to the base of tool holder, as illustrated in Figure A2.2. Another rectangular block, on which the micrometer is mounted, passes over the stainless tube and can be clamped into the desired position with a pair of nuts and bolts. The actual scratching tool is glued to the front end of the micrometer It may be recalled that there is a gap of 1.5 in. from the top of door opening and the top of the chamber (Figure4.1). This micrometer helps in positioning the tool below the beam. It was hoped to position the tool below the beam by a few trials. But it was realized later that the tip of the tool was below the detector even after fifteen trials and the tool tip always missed the detector by a few micrometers. It may be possible to bring it below the beam after a few more iterations, but it must be noted this had to be repeated for each and every experiment and this may damage the vacuum

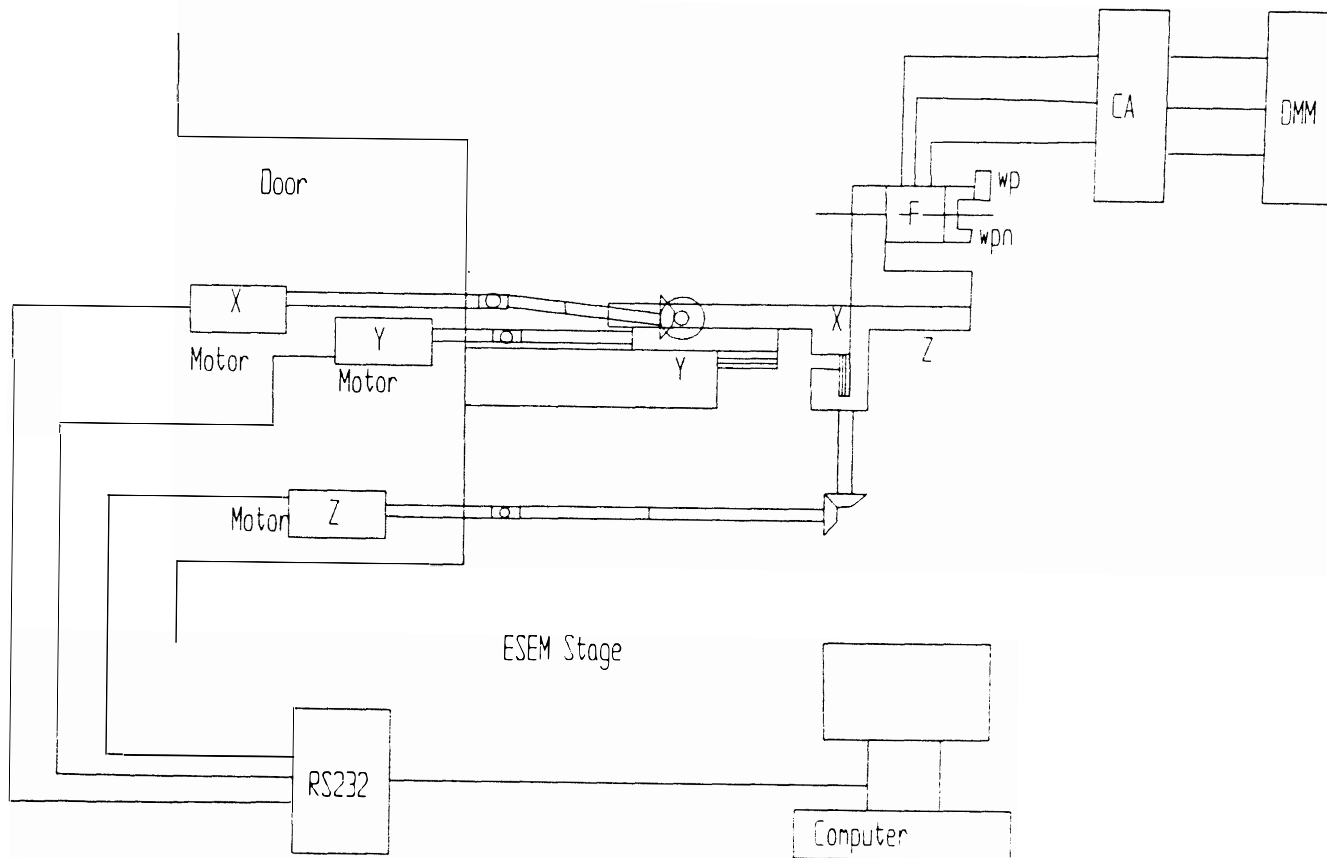

Figure 4.4. Schematic of the stage control and the force sensing circuit

system of the ESEM. Hence, it was decided to further modify the design. which led to the third design.

In the third design a separate scratching stage was built which would scratch without any of the motion of the ESEM stage and then use the X-, Y-, Z- motions of the stage to place the tool below the detector and control the movements of the scratching stage externally.

Third Design

Figure 4.6 is a schematic of the *in-situ* scratching apparatus with the complete force circuit. The force sensing circuit is the same as in the first two designs. The whole set up is mounted on the stage of the ESEM in place of table T. Figure A2.3 is the assembly drawing of the *in-situ* scratching stage and Figures A.2.4 to A.2.10 are various parts, such as the base plate, the workpiece holder, the ball screw assembly mounting plate, the tool holder, the piezomount, precision ball screw assembly, and ultra precision linear slide. The work material (glass slide) is glued to the work mount by an epoxy resin. The work mount is mounted on to the nut of the precision ball screw assembly. The precision ball screw is powered by a geared dc motor. The speed of the motor can be varied by a variable dc power supply to a maximum of 36 rpm. The bottom of the work mount is coupled to an ultraprecision linear slide to obtain a straight scratch. The ultra precision linear slide is in turn fastened to the base plate. The ball screw assembly is held on a ball screw mounting plate (Figure 4.6) which is fastened to the base plate. The scratching tool is held stationary so that it can be focused under the beam of the ESEM, and the work moves back and forth to facilitate the scratching operation. The workpiece can be moved back and forth by changing the polarity of the motor. The scratching tool is clamped to the tool holder with the help of a screw. A Kistler 3-component piezoelectric dynamometer is sandwiched between the tool holder and the

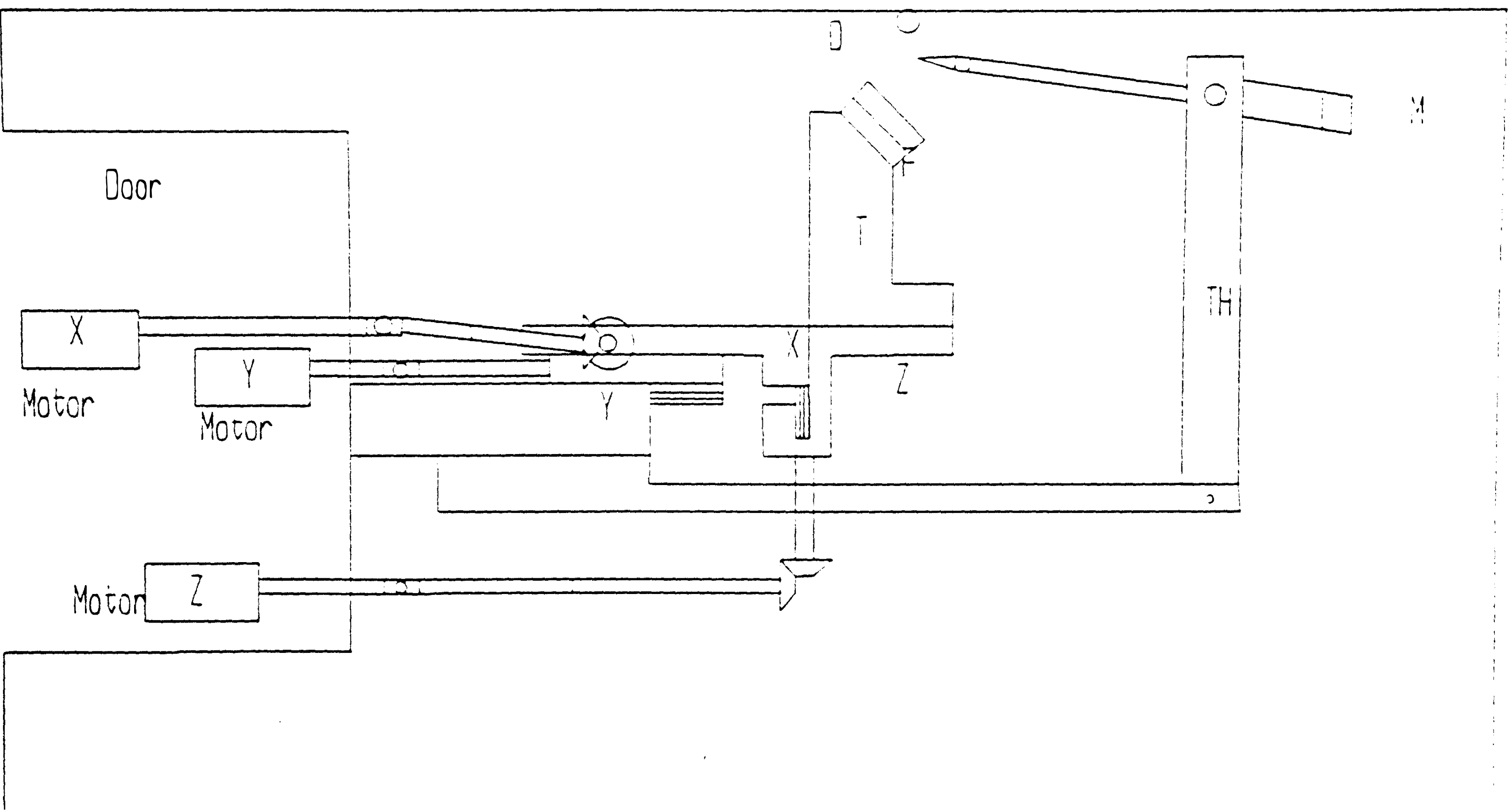

Figure 4.5. Schematic of second design

support base (see Figure 4.6 for details), and all the three components are preloaded with a bolt and a nut. The support base in turn is mounted on the piezoelectric actuator which controls the scratching depth and the forces induced during scratching. The expansion of the piezo actuator is controlled by the piezo controller. The piezo actuator is mounted on the piezo mount (Figure 4.6) which is fastened to the base plate. The set up is mounted on to the stage of the ESEM. Motions in X-, Y- and Z- axes facilitate focusing of the beam on the tool tip and allow the observation of scratching *in-situ* .

The chamber has both BNC and pin terminals. So, dc motor and piezoactuator can be controlled from outside. Similarly, the outputs from the dynamometer can be fed into charge amplifiers, located outside the chamber. Thus scratching and positioning can be controlled from outside the chamber when the system is under vacuum.

The technical details of the dynamometer, charge amplifier, piezo controller, precision ball screw assembly, and ultraprecision linear slide, calibration of dynamometer, and voltage versus speed of workpiece graph are given in the appendices.

This design is able to meet all the requirements imposed and performs satisfactorily. *In-situ* scratching tests were performed on glass at two cutting speeds and two depths of cut, and recorded on video. The scratched surfaces were also examined in a conventional SEM after coating with Au-Pd for further analysis. Although the videos were satisfactory, individual photographs from them were not of high quality. The experimental procedure and test results are presented in the next chapter.

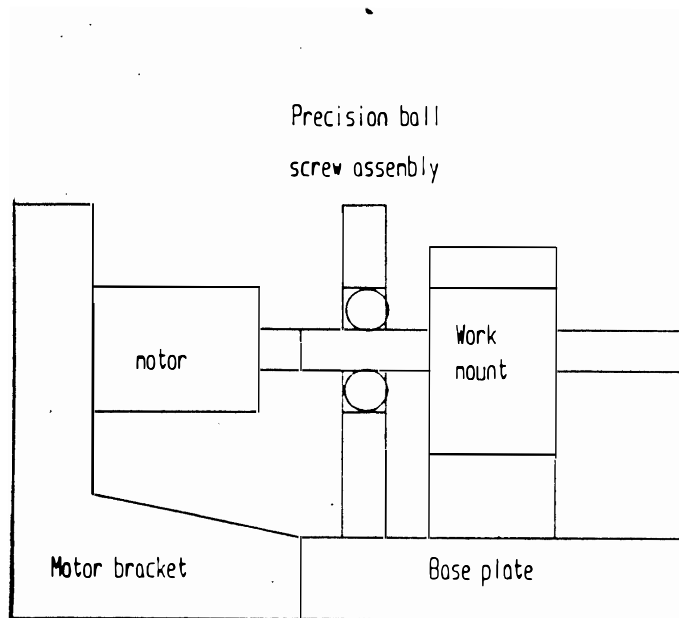

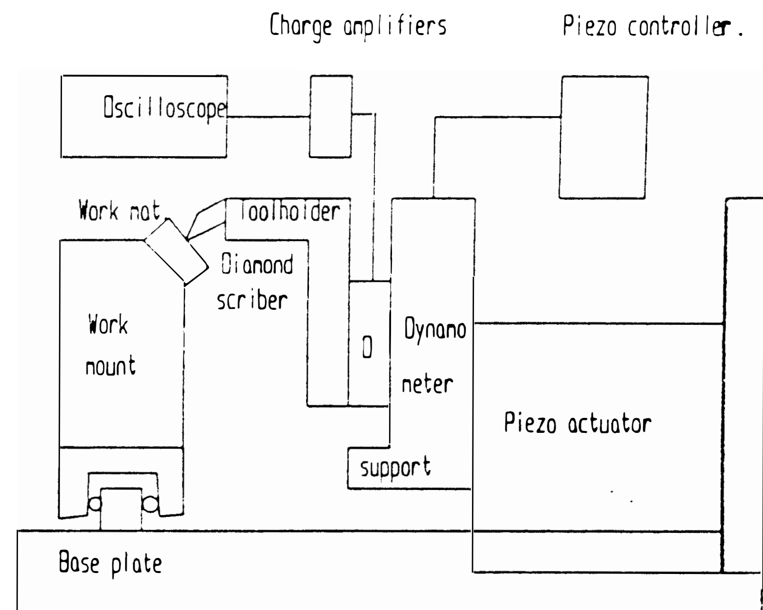

Figure 4.6. Schematic of third design

CHAPTER V

EXPERIMENTAL PROCEDURE AND TEST RESULTS

Experimental Procedure

1. The workpiece is glued to the workpiece holder using a resin.

2. All connections, namely, force transducer, piezoactuator control, and speed control are made.

3. The tool is clamped in the tool holder such that the tool tip just touches the glass workpiece.

4. Cutting force is applied by expanding the piezo actuator (by operating the piezo controller).

5. Cutting motion is given to the workpiece, relative to the tool, by increasing the voltage of the dc supply.

6. Forces are recorded in the X- and Y- directions and the scratching process is taped using a sony video casette recorder.

7. The specimen is then coated with Au-Pd and viewed in a conventional SEM to obtain micrographs for higher resolution.

Test Results

At light loads, the *In-situ* scratching apparatus produced grooves without causing any surface damage. The scratching process can be observed as it progresses, viewed upto a magnification of 500 X. Above this, the tool covers the whole of the TV monitor. This setup satisfies all the constraints imposed by the ESEM. In the following, scratching experiments inside ESEM, with a tool of 115° cone angle

are reported for two sets of conditions (Table 5.1), and two additional sets of experiments, along with the ones reported in Table 5.1 were performed outside the ESEM and are given in Table 5.2.

Table 5.1 Cutting conditions inside the ESEM

Speed	Load
Low speed (0.143 mm/sec)	Low (avg) load (0.034 N)
	Avg. Load for material fracture (0.15 N)

Table 5.2 Cutting conditions inside the ESEM

Speed	Load
Low speed (0.143 mm sec)	Low avg. load (0.034 N)
	Load for material fracture (0.15 N)
High speed (0.52 mm/sec)	Low avg. load (0.035 N)
	Load for material fracture (0.2 N)

Higher speed scratching experiments were also conducted inside the ESEM but were not reported because they had to be viewed at higher scan rates which reduced the quality of the image significantly. The results of the scratching experiments are now discussed in detail.

Low Speed - Low Load Tests : Here the minimum possible load and velocity were applied. Under these conditions, it was possible to form grooves without fracturing the surface. Figure 5.1 is a SEM micrograph illustrating material flow taking place as the workpiece came into contact with the tool. Figure 5.2 is an SEM micrograph

illustrating a representative surface of the whole scratch length. It can be seen that clean grooves can be formed and there is no evidence of surface cracks at this magnification. Figure 5.3 is an SEM micrograph showing the groove formed when scratching inside the ESEM under the same conditions, but with a sharp indenter (115 deg. cone angle). It can be seen that the groove is smooth and there is no evidence of surface cracks at this magnification. Also, note that there is some side flow.

Low Speed - Higher Load Tests : The normal load is increased by expanding the piezo actuator by 20 nm (which is the least count of the device) and scratching was performed. Here, the majority of the material removal was by brittle fracture but there was also some regions on the groove where material flow accompanied the fracture. Many chips were found in this region. Figure 5.4 is an SEM micrograph showing fractured portions of the groove and Figure 5.5 is an SEM micrograph at higher magnification of the same. It can be seen that considerable amount of material chipping had taken place. Figure 5.6 is an SEM micrograph of the debris formed due to brittle fracture along with a chip of approximately 80 μm length. Figure 5.7 is an SEM micrograph showing a mixed mode of material removal region. i.e., brittle mode of removal along with smooth groove (towards the right side in the figure). Long chip, measuring approximately 40 μm can also be seen. The chips appear wavy like a ribbon and are less than a μm wide. Figure 5.8 is an SEM micrograph showing another type of chip that is twisted and measuring approximately 100 μm. long.

High Speed - Low Load Tests: High speed here refers to the maximum speed that can be attained by the scratching set up. The results obtained here are very much similar to the low speed - low load scratching tests. Figures 5.9 and 5.10 are SEM micrographs showing representative grooves formed. Even though a single point tool is used, the radius of the tool is ≈16 μm and the tool is not perfectly smooth at the tip. It appears that the contour of the tool at the tip is formed on the grooved glass surface. There is no evidence

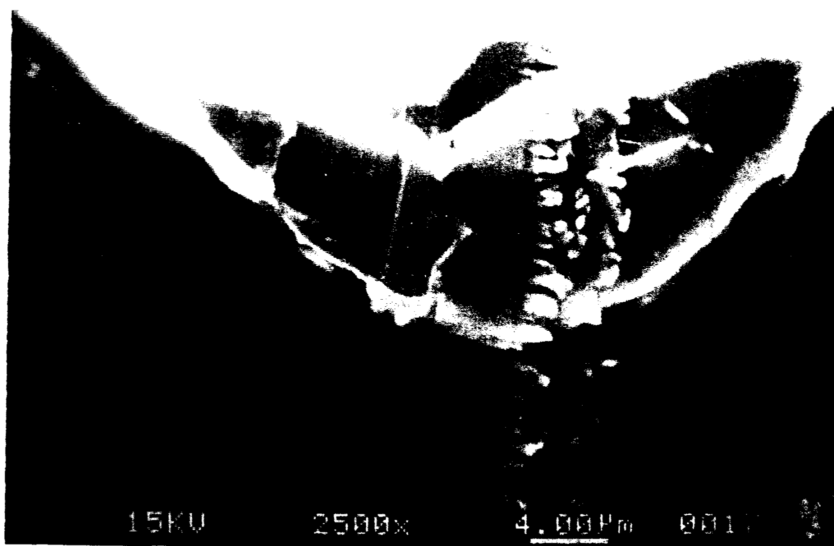

Figure 5.1. SEM micrograph showing material flow occurred when the work piece was struck by the indenter (Load:0.035 N and Scratching Speed: 0.143 mm/sec)

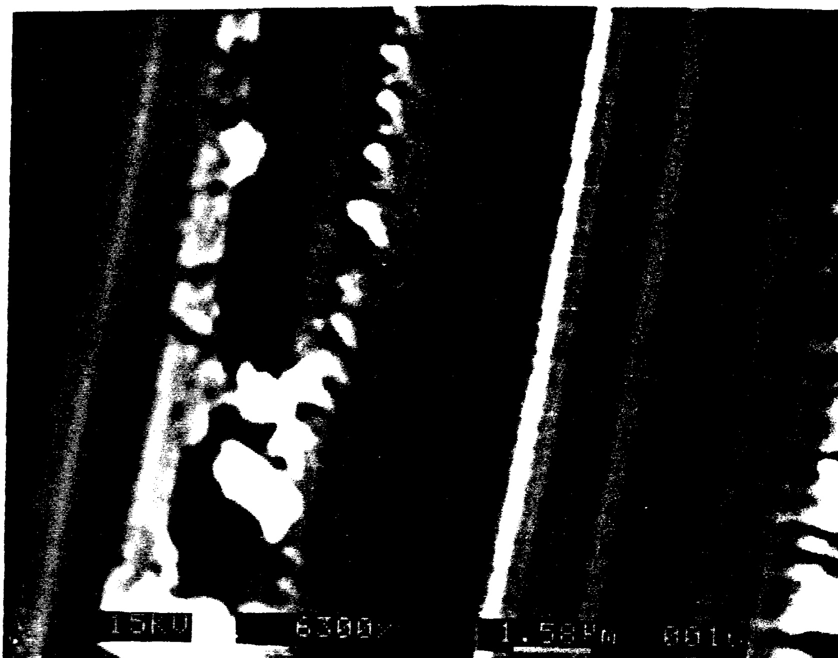

Figure 5.2. SEM micrograph of representative scratched groove surface (Load:0.035 N and Scratching Speed:0.143 mm/sec)

of surface cracks on the grooves at a magnification of 5500 X. There is side flow but no chip formation.

High Speed - Higher Load Tests: The results obtained here are also similar to the low speed - high load experiments. The major mode of material removal was brittle fracture, and there were zones of extensive chip formation accompanied by groove formation without cracks. Figure 5.11 is an SEM micrograph showing the heavily fractured surface (lower part) and crack free groove (upper part). It can be seen that brittle chippings are scattered all around the groove. Figure 5.12 is an SEM micrograph of the magnified view of the upper portion of the above figure. At higher magnification, burr like features are formed at the edge of the side flow, as shown in Figure 5.13. Figure 5.14 is an SEM micrograph showing a chip around 30 μm long. Here, there is a neat groove formation at the center and cracking at the edge of the groove. Figure 5.15 is an SEM micrograph showing a long chip seperating from the edge. As scratching proceeds, material is flown to the sides and this side flow gets separated as a long chip.

Experiments were also conducted under similar load and velocity conditions (as in 115 deg.) from another diamond tool of 75 deg. cone angle. The experimental conditions are tabulated below in Tables 5.3 and 5.4. The results formed here were very much similar to the previous set of experiments. Figure 5.16 is an SEM micrograph showing the groove obtained by low speed-low load scratching experiment. A smooth groove accompanied by side flow can be seen.

Table 5.3 Cutting conditions inside the ESEM 75° cone indenter

<table>
<tr><td rowspan="2">Low speed

(0.143 mm/sec)</td><td>Low load
(0.03 N)</td></tr>
<tr><td>Load for material
fracture (0.12)</td></tr>
</table>

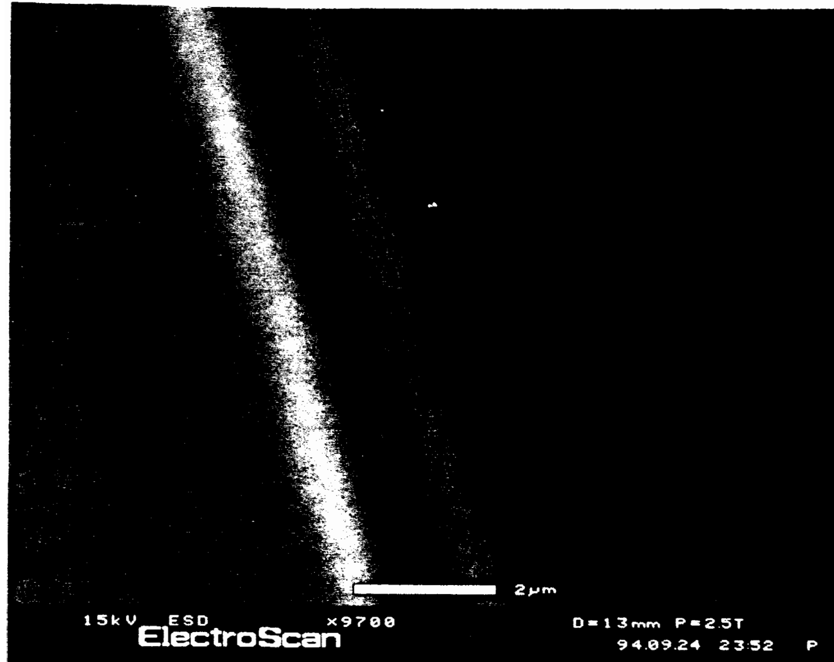

Figure 5.3. SEM micrograph showing smooth groove produced in the *in-situ* scratching mode (Load:0.035 N and Scratching Speed:0.143 mm/sec)

Figure 5.4 SEM micrograph showing a fractured surface generated at (Load:0.15 N and Scratching Speed:0.143 mm/sec)

Figure 5.5. SEM micrograph at higher magnification view of the crack produced in Figure 5.4

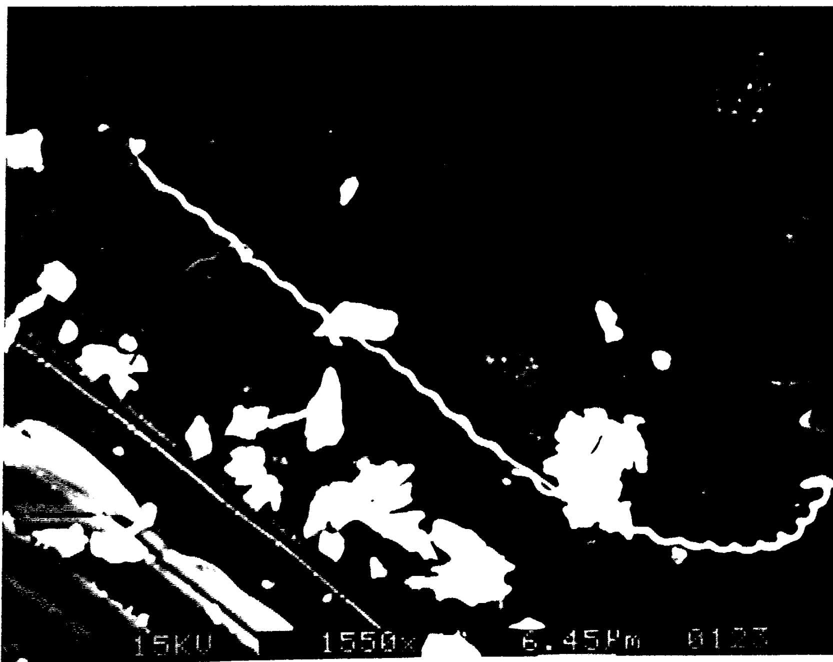

Figure 5.6. SEM micrograph of a chip measuring approximately 80 μm. (Load:0.15 N and Scratching Speed:0.143 mm/sec)

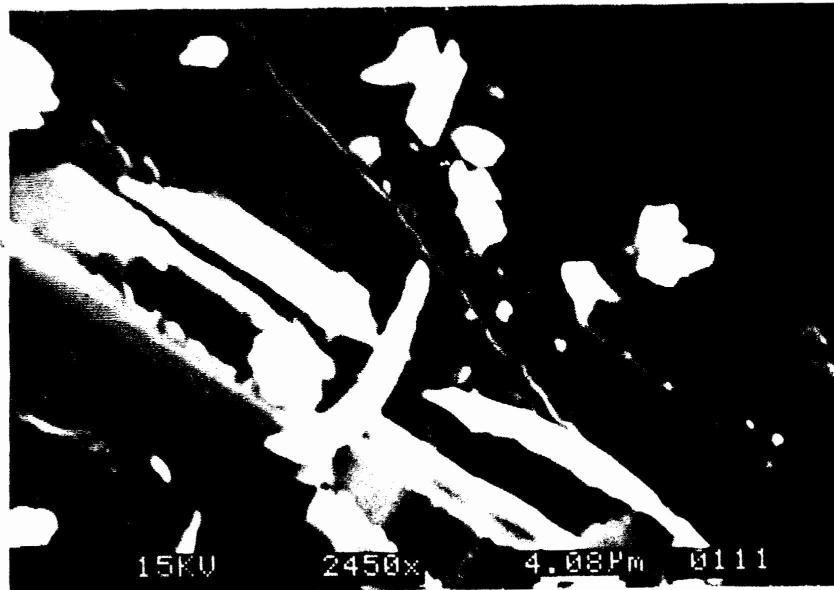

Figure 5.7. SEM micrograph showing a ribbon like chip measuring approximately 40 µm. (Load:0.15 N and Scratching Speed:0.143 mm/sec)

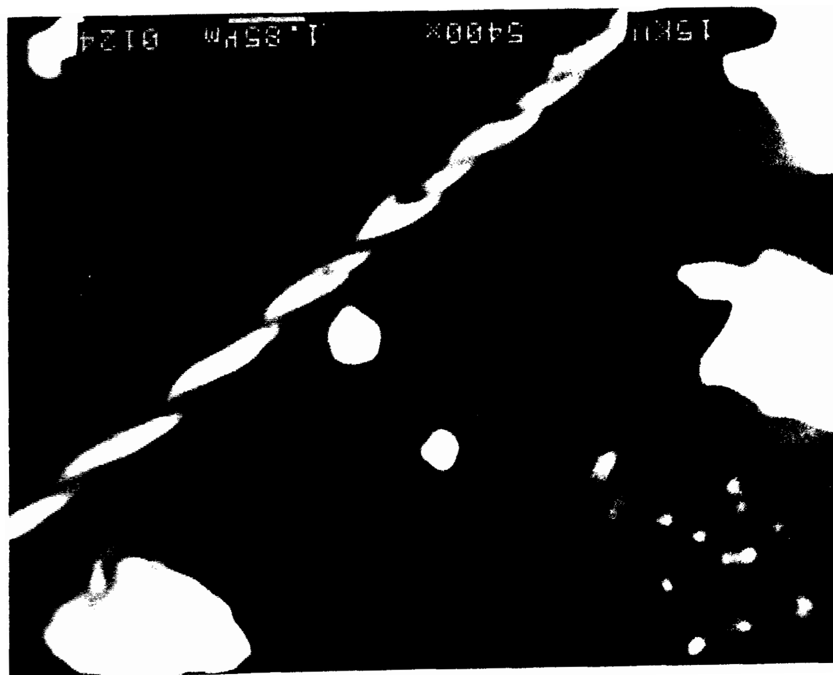

Figure 5.8. SEM micrograph of a twisted chip (Load:0.15 N and Scratching Speed:0.143 mm/sec)

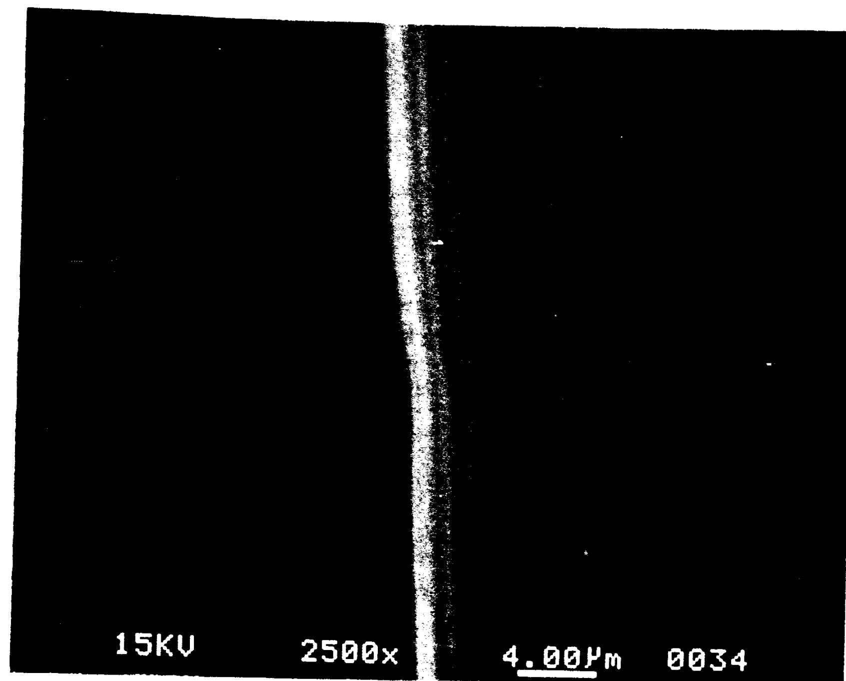

Figure 5.9. SEM micrograph of groove formed by 115 deg. indenter smooth grooves without microcracks can be seen (Load:0.15 N and Scratching Speed:0.52 mm/sec)

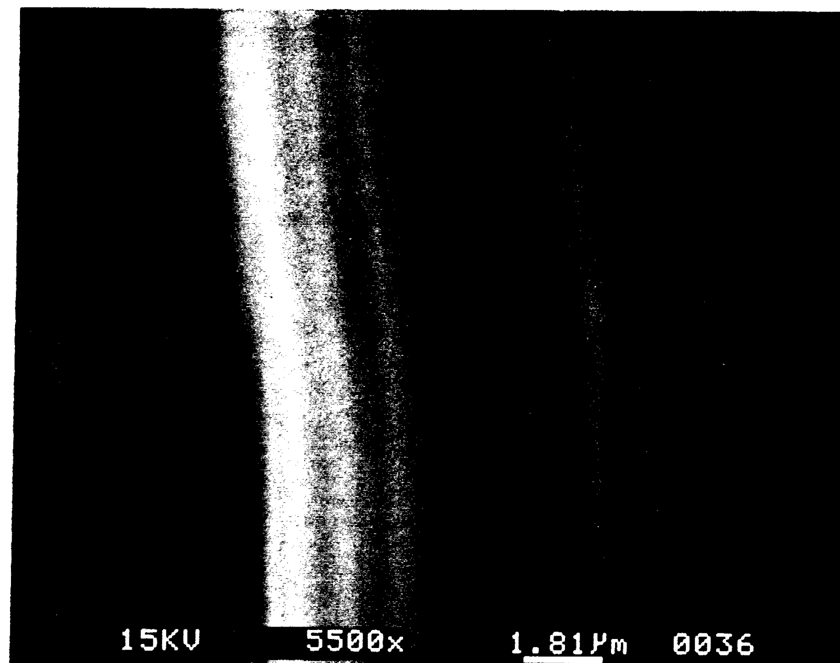

Figure 5.10. SEM micrograph showing higher magagnificaton view of the groove illustrated in Figure 5.9.

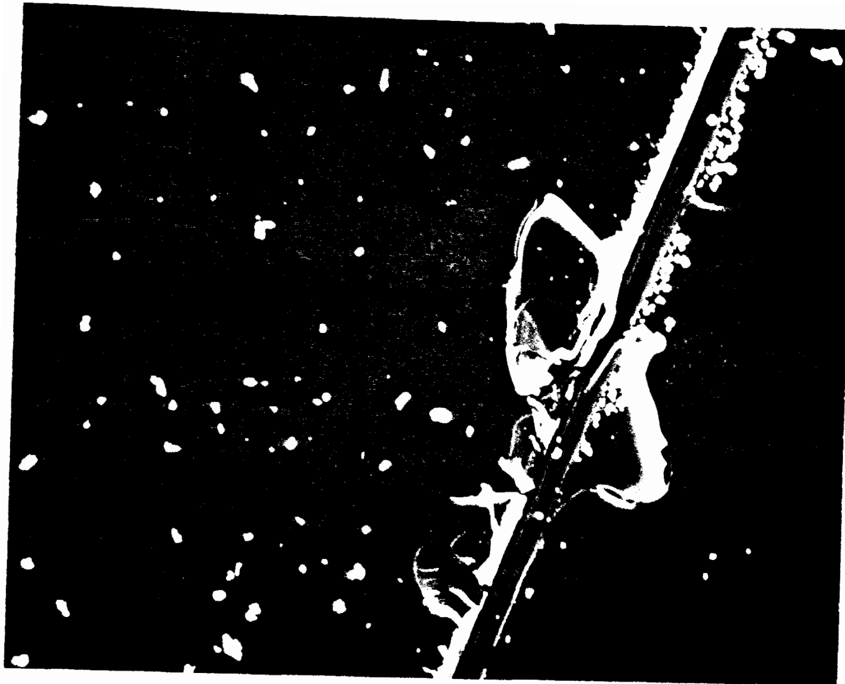

Figure 5.11. SEM micrograph showing overall view of the groove formed due to 0.2 N load and 0.52 mm/sec speed, showing fracture

Figure 5.12 SEM micrograph showing burrs at the edges of the groove formed during scratching

Figure 5.17 illustrates the overall view of the of surface scratched at low velocity and higher loads. A long chip measuring over

Table 5.4 Cutting conditions outside the ESEM 75° cone indenter

<table>
<tr><td rowspan="2">Low speed
(0.143 mm/sec)</td><td>Low load
(0.031 N)</td></tr>
<tr><td>Load for material fracture (0.15 N)</td></tr>
<tr><td rowspan="2">High speed
(0.52 mm/sec.)</td><td>Low load
(0.035 N)</td></tr>
<tr><td>Load for material fracture (0.17 N)</td></tr>
</table>

750 μm and a considerable amount of brittle fracture debris can be found. Figure 5.18 is an SEM micrograph showing at the higher magnification (3500 X) of a long chip illustrated above. Figure 5.19 is an SEM micrograph showing the overall view of scratch made at high load and high velocity. Flat ribbon like chips are seen in Figure 5.17. Brittle fracture and chips can also be seen on this groove. Figure 5.20 is an SEM micrograph of chips formed on the scratch groove, which are approximately 25 μm. long. Some points of interest observed during the preliminary scratching tests are illustrated from Figure 5.21 onwards. Figure 5.23 is an SEM micrograph showing another type of chip similar to one illustrated by the Schinker when machining glass at over 20 m/sec. The normal loads for the scratches shown in Figures 5.21, 5.11 and 5.23 was < 0.2 N and the velocity was not recorded but was some where in between the lowest and highest possible speed attainable by the equipment.

Figure 5.13. SEM micrograph of another kind of chip formed at 0.2 N load and 0.52 mm/sec scratching speed

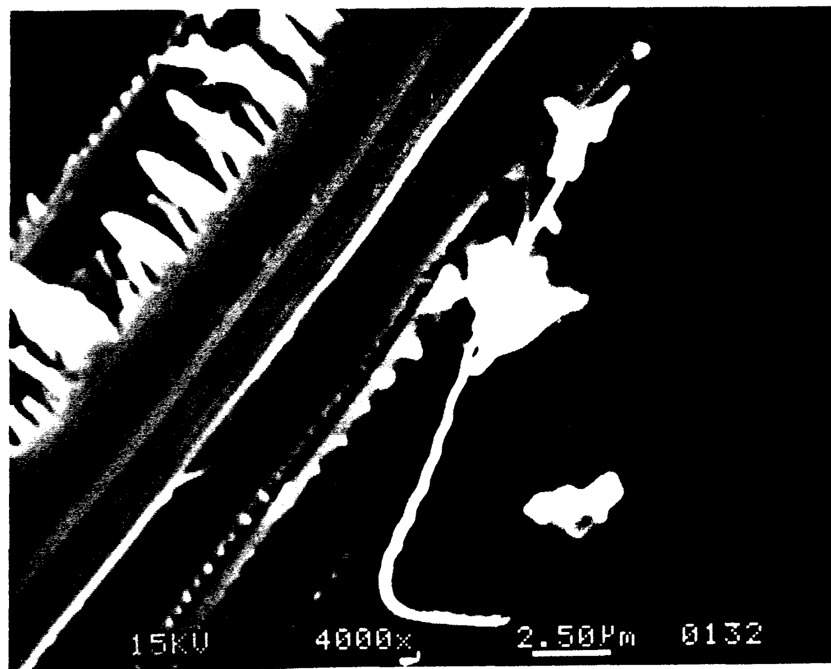

Figure 5.14. SEM micrograph showing a long chip measuring approximately 30 µm at conditions as in Figure 5.13

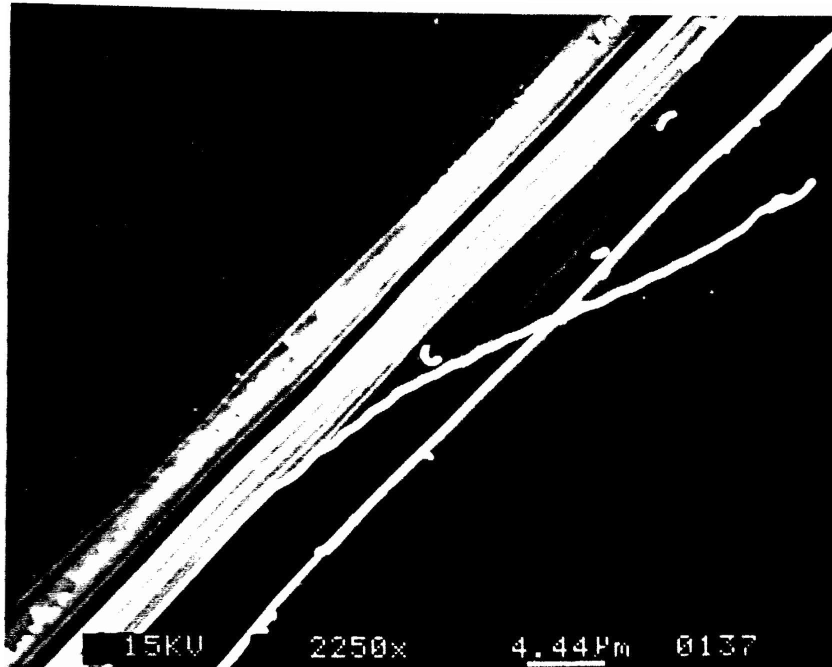

Figure 5.15. SEM micrograph at higher magnification showing long chip seperated from the side of the groove edge

Figure 5.16. SEM micrograph showing smooth grooves formed under low load and low velocity scratching with a 75° cone angle indenter

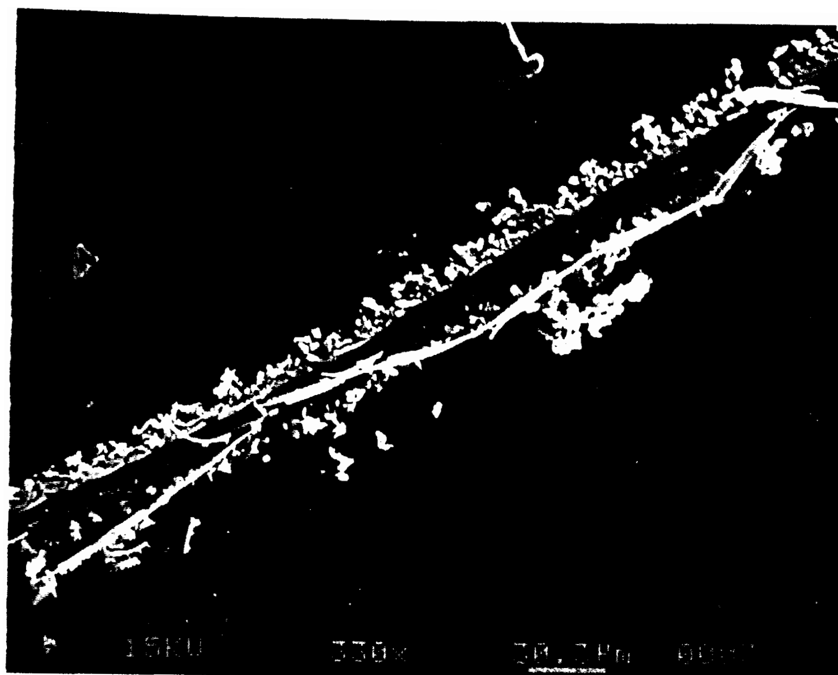

Figure 5.17. SEM micrograph of the overall view of low velocity and high load scratched surface with a 75° conical indenter

Figure 5.18. SEM micrograph of the chip shown in the Figure 5.17 at high magnification

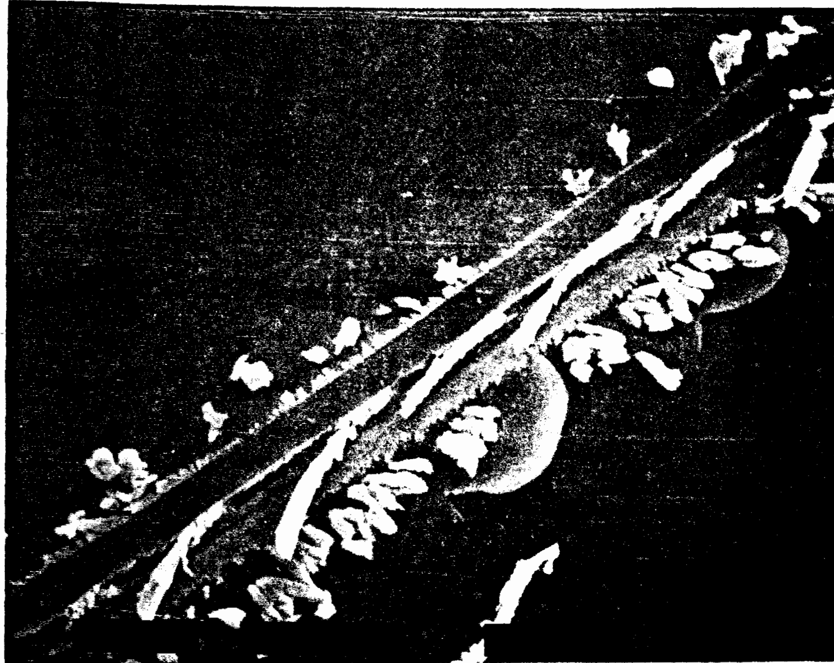

Figure 5.19. SEM micrograph of the overall view of groove formed at 0.2 N load and 0.52 mm/sec scratching velocity

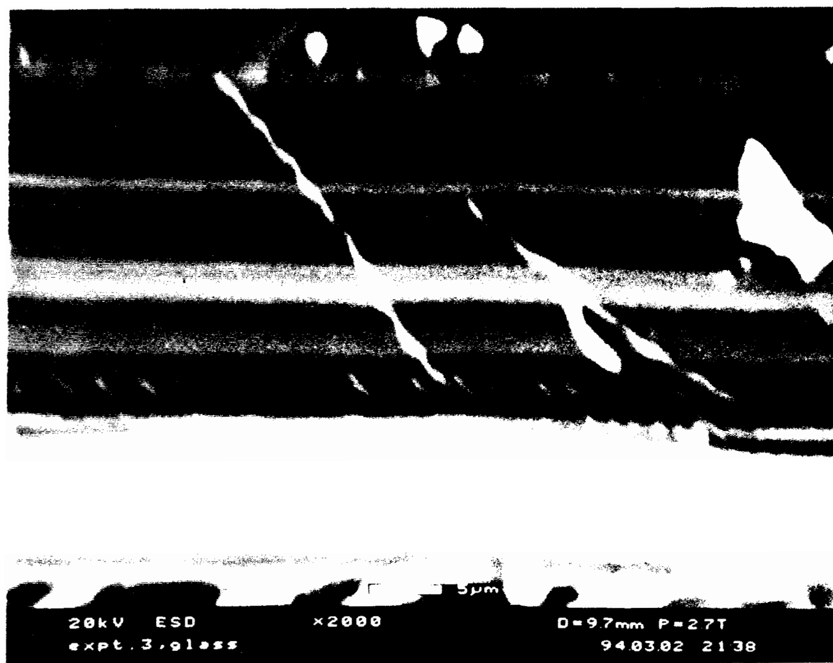

Figure 5.20. SEM micrograph of chips formed at high load and high velocity

Figure 5.21.An SEM micrograph of a chip that appears highly stressed formed at 0.2 N load

Figure 5.22.SEM micrograph of a brittle chip formed at 0.2 N load

Figure 5.23. SEM micrograph of another type chip

CHAPTER VI

DISCUSSION

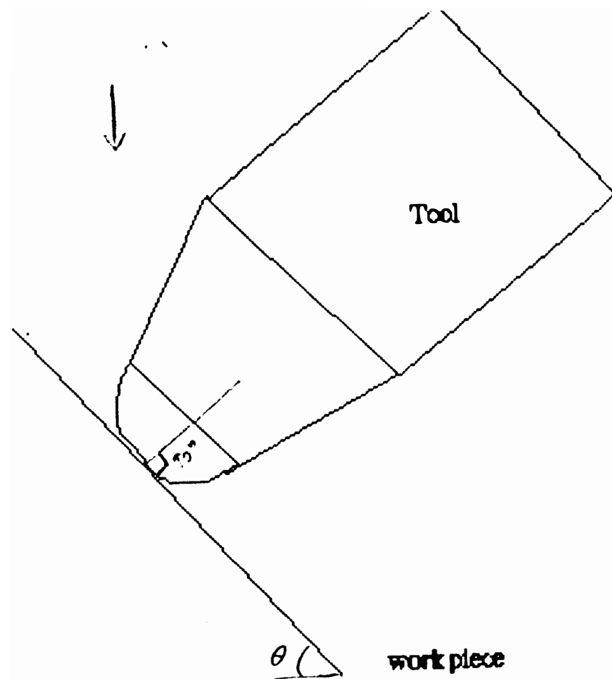

Figure 6.1 Tool tip and the workpiece at higher magnifications

This investigation has established the requirements needed to conduct *in-situ* scratching studies inside an ESEM.

The process imposes a certain restriction on the *in-situ* observation process. It can be seen from the Figure 6.1 that

work piece has to be inclined at some angle to the horizontal to facilitate viewing through ESEM. The complete tool radius does not come in contact with the work material during scratching but only one or more protruding points do the actual scratching. Hence when viewed from the top the tool itself hides the side flow formation.

Schinker [9] reported that formation of microcrack free grooves is not possible at scratching velocities < 20 m/sec. He reasoned that only above this scratching speed the temperatures in the cutting zone increase to facilitate removal of material viscoplastically. But chips that resemble the ones reported by Schinker are obtained in this investigation at very low speeds.

This investigation also shows that most of the chips that are formed are due to the separation of the material at the edges of the groove sideflow. It is observed from the low speed experiments that chips are not formed. This is because the sideflow may be getting separated due to stresses and the stresses must be insufficient for chip formation at lower loads.

In the higher load experiments, even though glass has cracked at some places along the groove, there has been stretches where microcracks are not formed even though the major mode of material removal there is brittle fracture (Figure 5.11). This supports partially the argument put forth by Blake and Scatterwood [7]. But Blake's argument does not explain the chip formation process.

From low load experiments microcrack free grooves and side flow formation can be seen. From high load experiments, it can be observed that surface cracks are produced, and there are stretches on the groove where material is removed by fracture, with no evidence of microcracks on the groove (Figure 5.12). Along with this side flow, chips are also observed in high load experiments. Hence, from the above observations and literature review, we can point out that, for normal loads ≈ 0.03 N a

microcrack free groove is formed due to material flow. and the area directly below the indenter being densified. For normal loads ≈ 0.15 N the groove formation is due to brittle fracture and material flow, with the area directly below the indenter is densified. The mechanism of material flow could not be determined in this investigation. Even though densification was not measured in this study, Ernsberger [6] and Peter [16] have demonstrated the densification effect when glass is indented by diamond.

CHAPTER VII

CONCLUSIONS

1. An *in-situ* stage for scratching inside the ESEM was designed, built and tested.

2. The transducer is capable of picking up dynamic forces of small magnitude (0.03N).

3. Piezo actuator is capable of giving small depths of cuts (upto 15 μm).

4. The magnet inside the dc motor is far enough, as to not effect the beam.

5. *In-situ* scratching has been observed upto 500 X magnification.

6. Scratching tests were conducted inside as well as outside the ESEM at different loads (≈0.03N and 0.2 N) and velocities (0.143 mm/sec and 0.52 mm/sec).

7. At low loads, microcrackfree grooves are formed at all scratching speeds and indenter geometries used. There is sideflow of material but no chip formation.

8. At higher loads cracks are observed at some places on the scratched surface. The major mode of material removal is by brittle fracture. Along the edges of the groove there is some sideflow and formation of long chips.

9. At the two scratching speeds used in this investigation the scratching process seems to be independent of speed. This is understandable considering the narrow range of speeds that can be used inside ESEM.

10. Grooves can be viewed immediately after their formation in *in-situ* scratching inside the ESEM. However, the formation of sideflow and chips in could not be observed because the actual tool and workpiece contact area was shielded by the tool itself.

CHAPTER VIII

RECOMMENDATIONS FOR FUTURE WORK

1. A finer indenter should be used in the *in-situ* scratching experiments inside the ESEM in order to facilitate the observation of grooving

2. The scratching setup should be further modified by facilitating a macro tool movement, real time touch sensor and feed back control

3. *In-situ* scratching studies should be extended to brittle materials such as silicon nitride, silica, aluminium oxide, germanium, etc to study the mechanism of microcrack free grinding.

4. Develop an analytical model for microcrackfree scratching of brittle materials which can predict the scratching process completely, by knowing the scratching parameters.

REFERENCES

1. Delingat, E. W., "The Production of Optical Surfaces : Survey of Present Technique and Preview on New Developments, "Symposium of Optical Surface Technology, SPIE, 381 (1983) 2

2. Evans, A. G. and D. B. Marshall., "Wear Mechanisms of Ceramics," Fundamentals of Friction and Wear, Published by ASM Int. (1980) 39

3. Taylor, E. W., "Deformation of Optical Glass," Nature 16 (1949) 323

4. Kendal, K., "Complexities of Compression Failure," Proceedings of Royal Society of London, 316A (1978) 245-263

5. Marsh, D. M., "Plastic Flow and Fracture of Glass," Proceedings of the Royal Society London, 282 A (1964) 33-43

6. Ernsberger, F. M., "Role of Densification of in Deformation of Glass Under Point Loading," J of American Ceramic Society, 51 (1968) 545 -547

7. Blake, P. N. and Scattergood, R. O., "Ductile Regime Machining of Germanium and Silicon," J of American Ceramic Society, 73 (1990) 949-957

8. Putttick, K. E., Rudman, M. R., Smith, K. J., Franks, A. and Lindsey, K., "Single Point Diamond Machining of Glasses," Proceedings of the Royal Society London, A426 (1989) 19-29

9. Schinker, M. G., "Basic Investigation Into High Speed Processing of Optical Glasses With Diamond Tools," A Symposium on Optical Surface Technology, SPIE 381 (1983) 32-38

10. Peter, K., Glastech.Ber, 37 (1964) 333

11. Van Vlack, "Engineering Materials," Addison-Wesley Publishing Company, (1975)

12. ASM Engineering Material Handbook, 4 (1991)

13. Komanduri, R. and Ramamohan, T. R., "On the Mechanism of Material Removal in Fine Grinding and Polishing Of Advanced Ceramics and Glasses," Japan Society for Precision Engineering (1994) K38-K50

14. Lawn, R., "Fracture of Brittle Solids," Cambridge University Press (1975) 75

15. Anisworth, L., "Diamond Pyramid Hardness of Glass in Relation to Strength and Structure of Glass - I, II and III," ibid, 38 (1954) 479-501, 536

16. Peter, K., "Densification and Flow Phenomena of Glass in Indentation Experiments," J of Non-Crystalline solids, 5 (1970) 103- 115

17. Hureta, M. and Malkin, S., "Grinding of Glass: The Mechanics of the Process," Transa ASME, J of Engg for Industry, 6 (1976) 459-467

18. Golini, D. and Jacobs, S. D., "Physics of Loose Abrasive Microgrinding," Applied Optics, 30 (1991) 2761-2777

19. Chandramauli, V., "An Analysis of Indentation of Brittle Materials," M. S. Thesis, Oklahoma State University (1992) 5

20. Broese van groenou, A. and Veldkamp, J. D. B., "Grinding Brittle Materials," Phillips Technical Review, 38 (1979) 105

21. Hagan, "Cone Cracks Around Vickers Indentations in Fused Silica Glass," J of Material Science, 14 (1979) 462-466

22. Bifano, T. G., Dow, T. A.and Scattergood, R. O., "Ductile - Regime Grinding: A New Technology for Machining Brittle Materials," Intersociety Symposium on Machining of Advanced Ceramic Materials and Components, American ceramic society, (1988) 113-120

23. Bifano, T. G. and Fawcett, S. C., "Specific Grinding Energy as an in Process Control Variable for Ductile-Regime Grinding," Precision Engineering, 13 (1991) 256-262

24. Bifano, T. G. and Yi, Y., "Acoustic Emission as an Indicator of Material-Removal Regime in Glass Micro-Machining," Precision Engineering, 14 (1992) 219-228

25. Komanduri, R., unpublished report, (1991)

26. Bridgman, P. W., "Effects of Very High Pressure on Glass," J of Applied Physics, 24 (1953) 405-413

27. Puttick, K. E., Shaihd, M. A. and Hosseini, M. M, "Size Effects In Abrasion of Brittle Materials," J of Applied Physics, D12 (1979) 195- 202.

28. P.I. Products of Micropositioning: Catalogue, (1994) 4.2

29. Kistler 9251A Technical Catalog, (1992)

30. Kistler 5004e Technical Catalog, (1992)

31. Berg Industries Product Catalog, B92, (1994) E384

32. NSK catalog, Precision Machine Parts and Linear Motion Products, pr.# A1371b, (1994) A122, A177

33. Servo Systems Co. Catalog, (1992) 15

34. Komanduri, R., Hayashi, S. R., Fielding, J. O and Bolon, "A Specimen Stage for *In-Situ* Orthogonal Machining Studies Inside SEM," Corporate R&D report # 80, CRD071 (1980)

35. Ramalingam, S. and Bell, A. C., "A SEM Stage for the Observation of Chip Formation," Rev.Sic. Instrum, 44 (1973) 573-576

36. Cahn, R. W., Haasen, P. and Krammer, E. J., "Glasses and Amorphous Material," Materials Science and Technology, 9 (1991)

37. Tomozawa and Doremus, "Treatise of Material Science and Technology-Glasses III," 9 (1992)

38. Hagan, "Shear Deformation Under Pyramidal Indentations In Soda Lime Glass," J of Material Science, 15 (1980) 1417-1424

39. Maan, N. and Broese van groenou, A., "Low Speed Scratching Experiments on Steels," Wear, 42 (1977) 365

40. Misra, A. and Finne, I., "On the Scribing and Subsequent Fracturing of Silicon Semiconductor Safer," J of Material Science, 14 (1979) 2567

41. Yoffe, E. H., "Elastic Stresses Caused by Indenting the Brittle Materials," Philosophical Magazine, 46 (1982) 617

42. Chen, S. Y., Farris, Chandrashekaran, "Sliding Microindentation Fracture of Brittle Material,"Tribology Transactions, 34 (1991) 161 -168.

43. Blake, P. N., Bifano, T. G., Dow, T. A and Scattergood, R. O., "Precision Machining of Ceramic Materials," American Ceramic Society Bulletin, 67 (1988)

44. Kirchner, H. P., "Comparison of SinglePoint and Multipoint Grinding Damage in Glass," J of American Ceramic Society, 67 (1984) 347-353

45. Cook, R. F., Lawn, B. R., Dabbs, T. P. and Chantikul, P., "Effect of Machining Damage on the Strength of a Glass-Ceramic," J of American Ceramic Society (1981) C121-C122

46. Bifano, T. G., Dow, T. A. and Scattergood, R. O, "Ductile-Regime Grinding of Brittle Materials : Experimental Results and Development of a Model," SPIE, 966 108-115

47. Miyashata, M., First Annual Precision Engineering Conference, (1985)

48. Lawn, B. and Wilshaw, R., "Review of Indentation Fracture: Principles and Application," J of Material Science, 10 (1975) 1049

APPENDIX A1

Environmental Scanning Electron Microscope

Figure A1.1 is a schematic of the pumping system and electron optics of the ESEM. Specimen chamber is maintained at a vacuum of 0.1 to 50 torr. Pumps at each stage maintain a pressure gradient which stops contaminants reaching the upper column, thus enabling the specimen chamber to be held at higher pressures. The electron optical column is maintained at high vacuum (10^{-6} torr). ESEM possesses an advanced computer software system that enables improved signal processing and image enhancement. Also, the ESEM chamber allows hot samples (upto 1000° C) in the presence of liquids and gases, to be viewed in their natural states.

The principle of operation of ESEM is shown in Figure A1.2. Only a fraction of the beam electrons are scattered into a diffused skirt. if the path length through the high pressure region is kept short enough (4-6 mm), the remainder of the electrons are used to form the image. Secondary electrons are evolved when the primary beam strikes the sample. Secondary electrons strike gas ions cascading the signal, which is then collected by a detector and displayed on a TV monitor. Charges on the sample is neutralized by the positive gaseous ions, permitting the sample to be viewed in its natural state without any conductive coating.

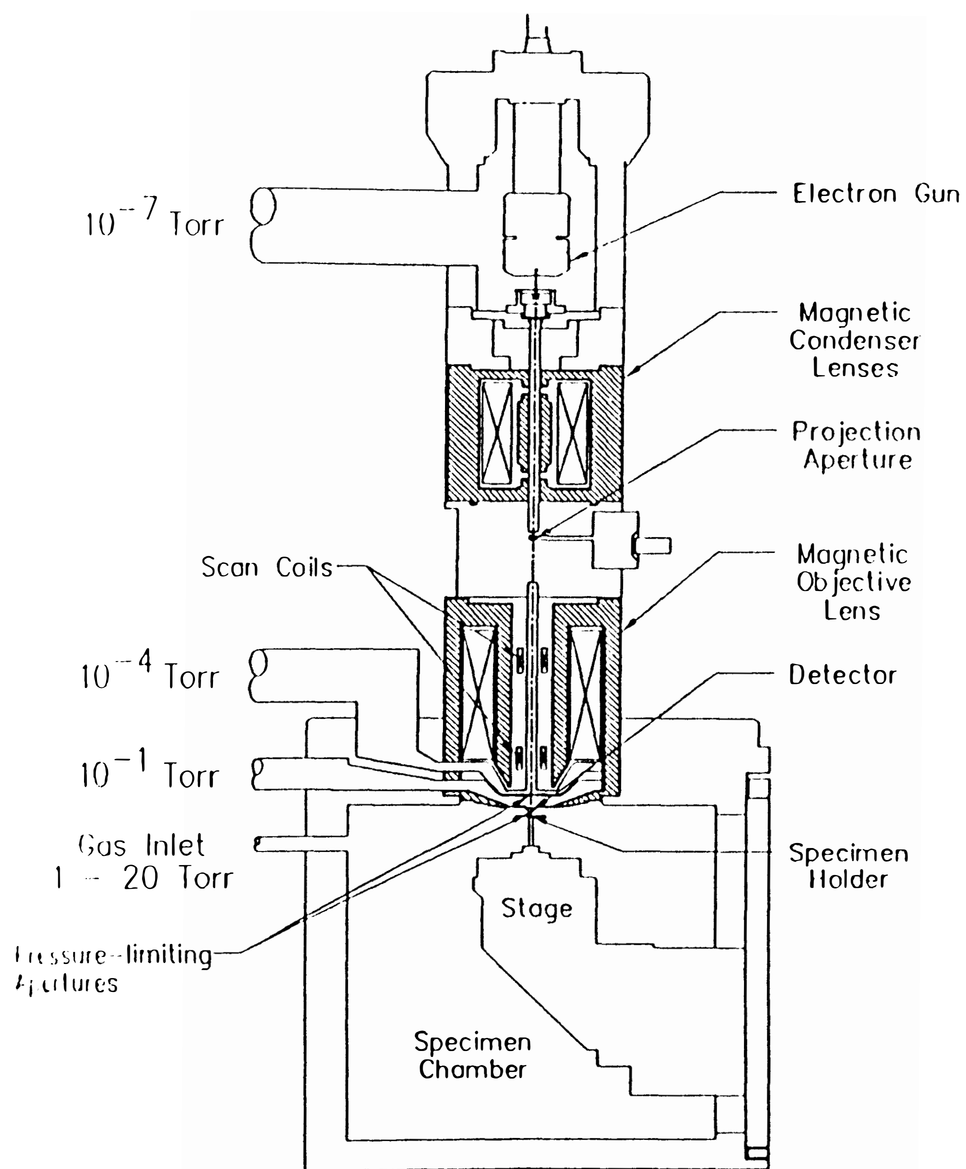

A1.1 Schematic of the ESEM showing pumping system and electron optics

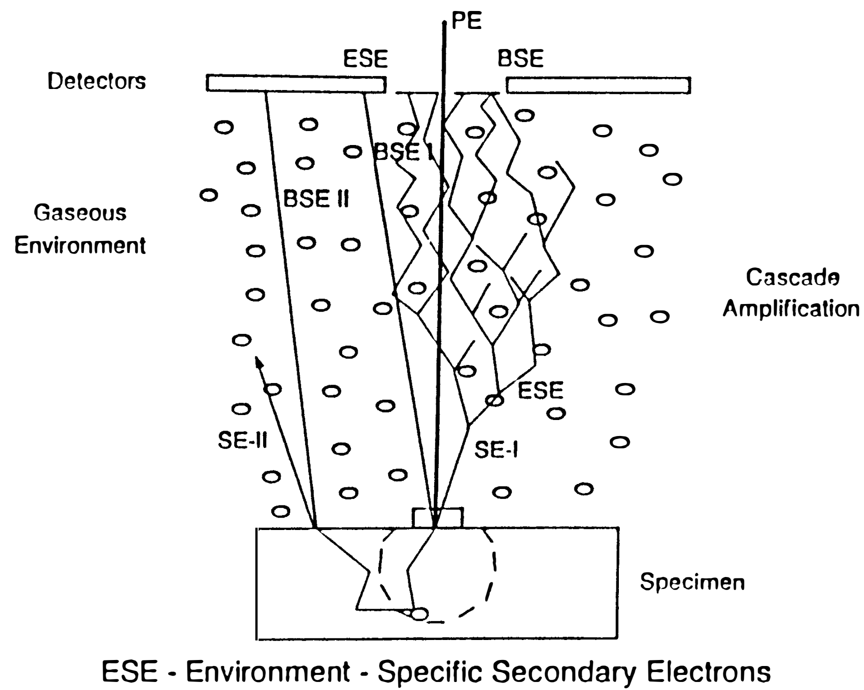

Figure A1.2 Schematic showing principle of signal production and collection

APPENDIX 2

Details of components used in scratching apparatus

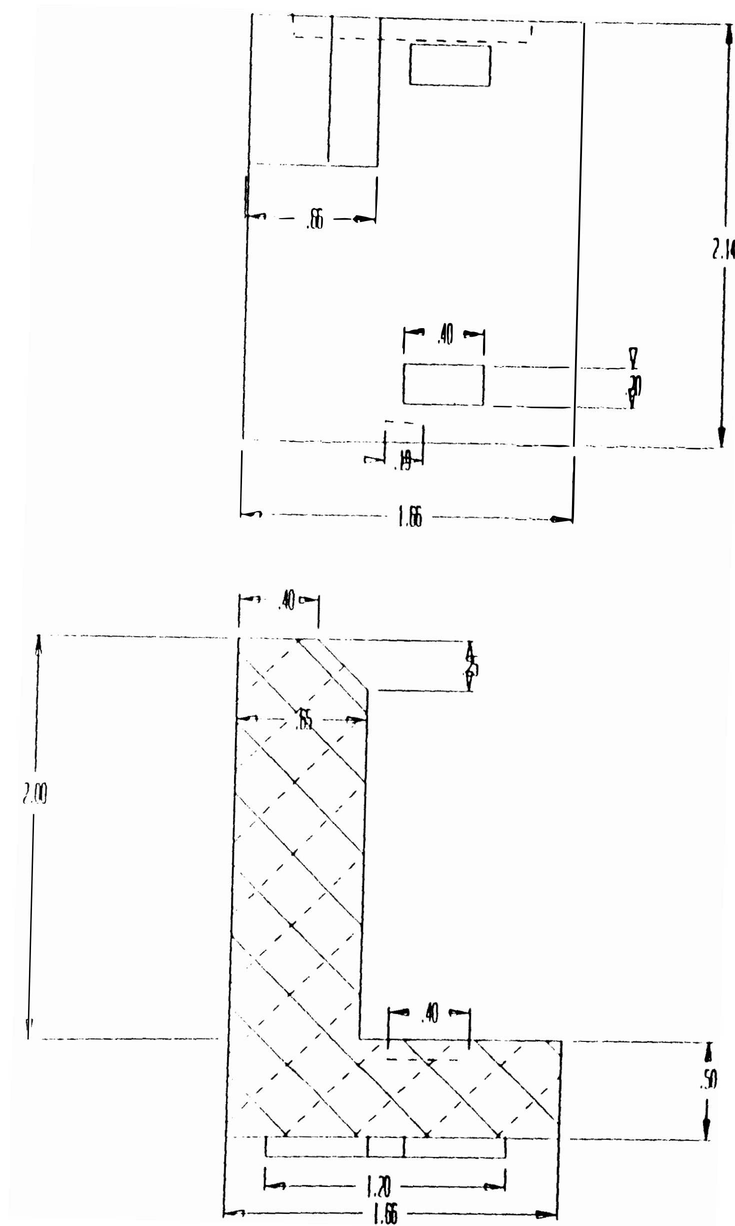

Figure A2.1 Detailed dimensions of table T

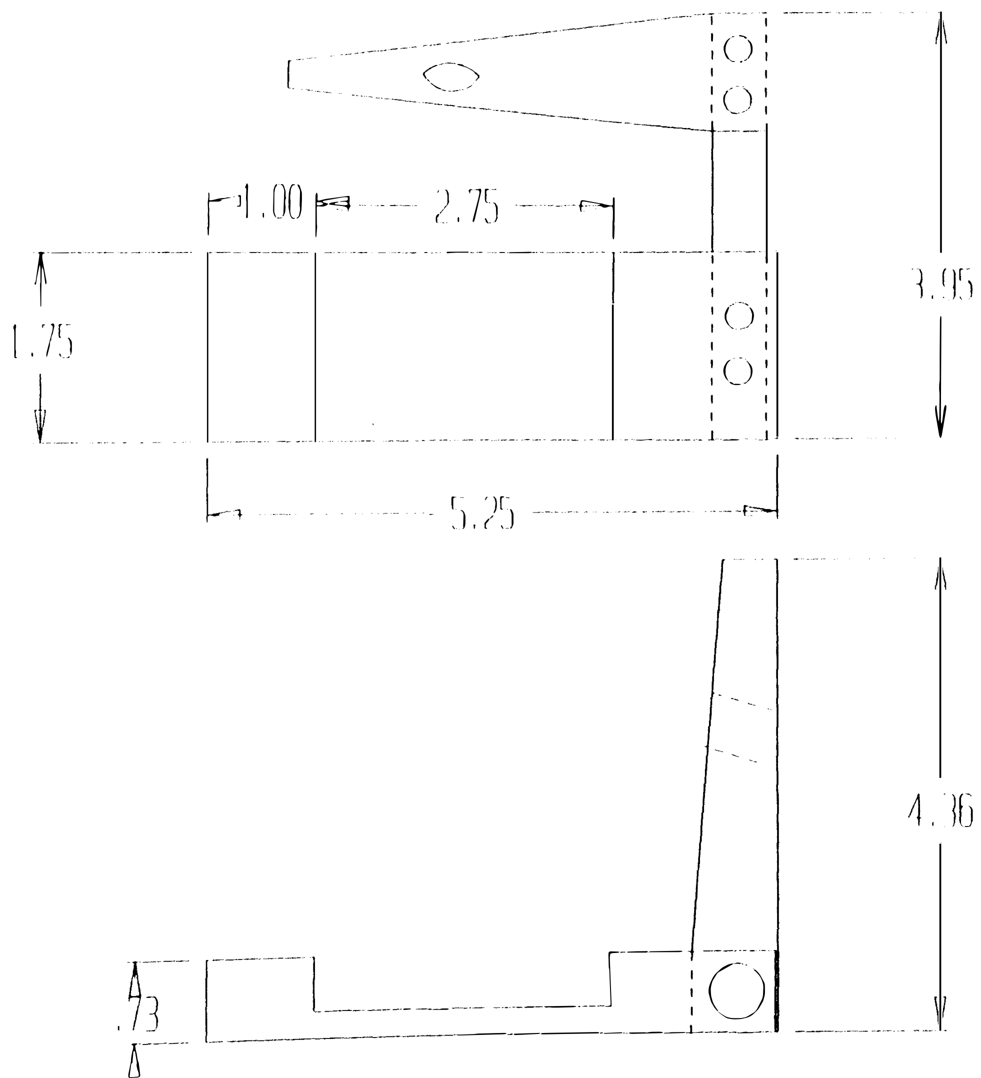

Figure A2.2. Detailed drawing of the tool holder

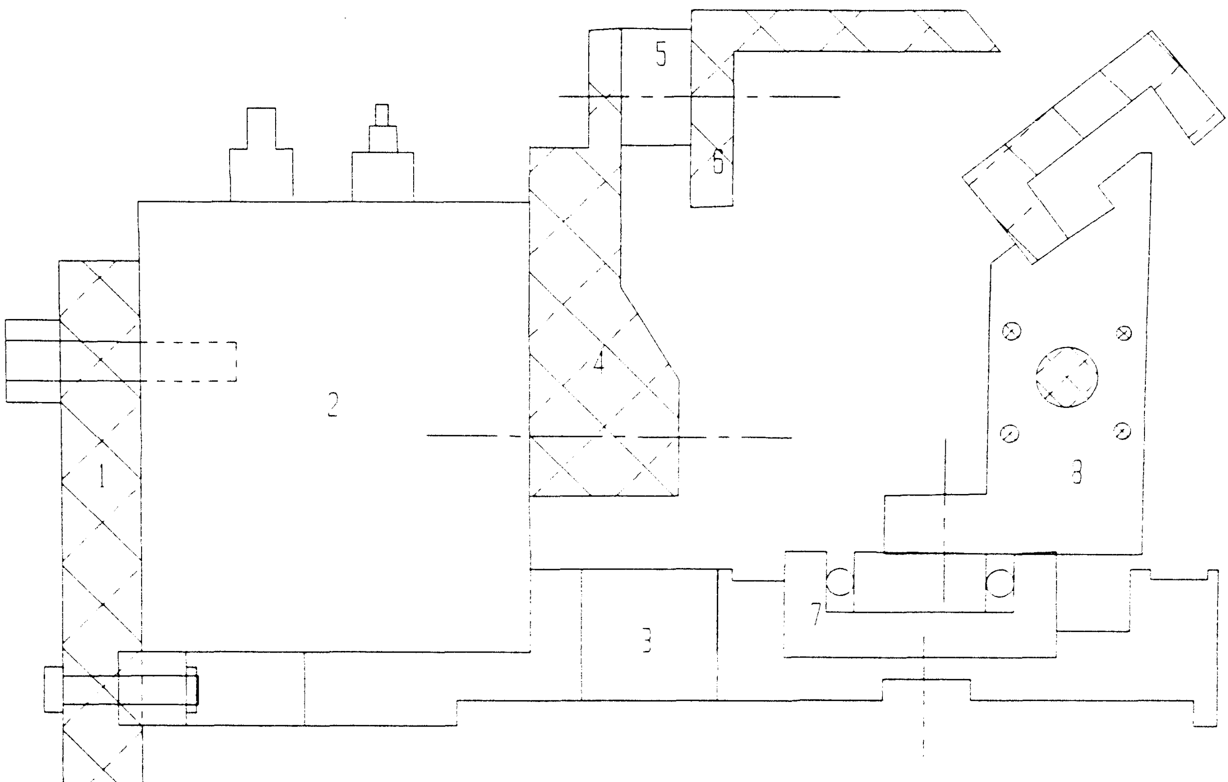

1. Piezo holder
2. Piezo actuator
3. Base plate
4. Dynamometer holder
5. Dynamometer
6. Tool holder
7. Ultraprecision linear slide
8. Tool holder
9. Precision ball screw assembly

Figure A2.3 Front view of third design

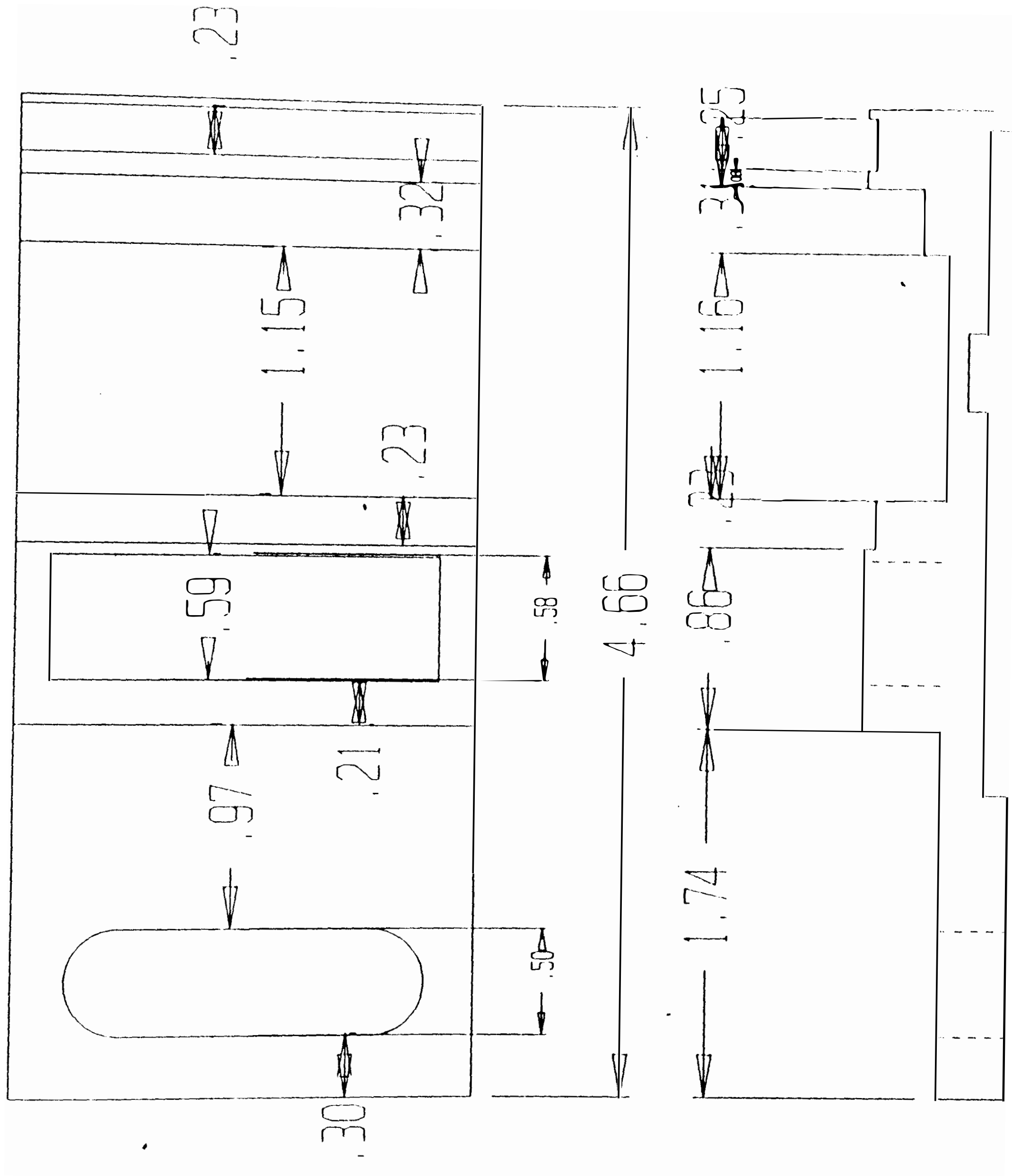

Figure A2.4. Base plate

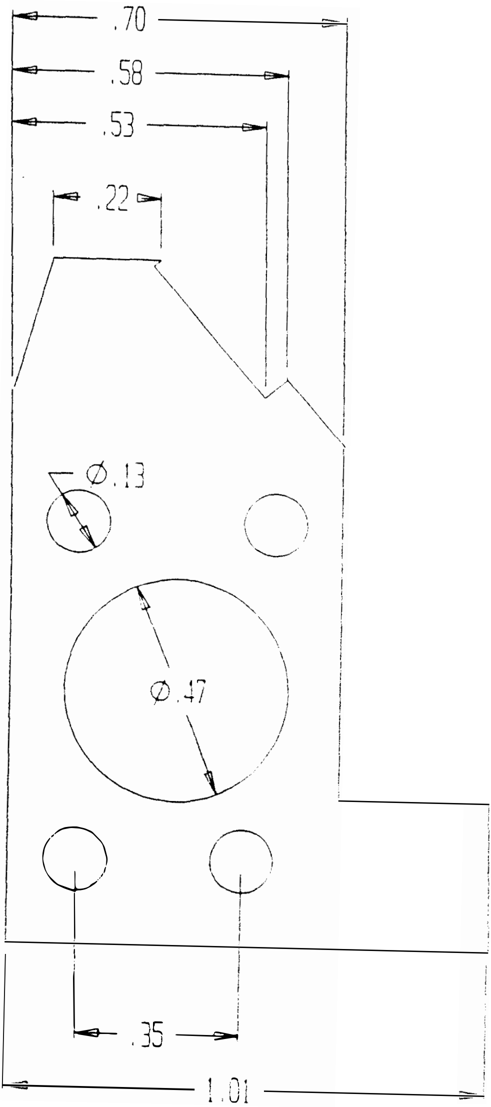

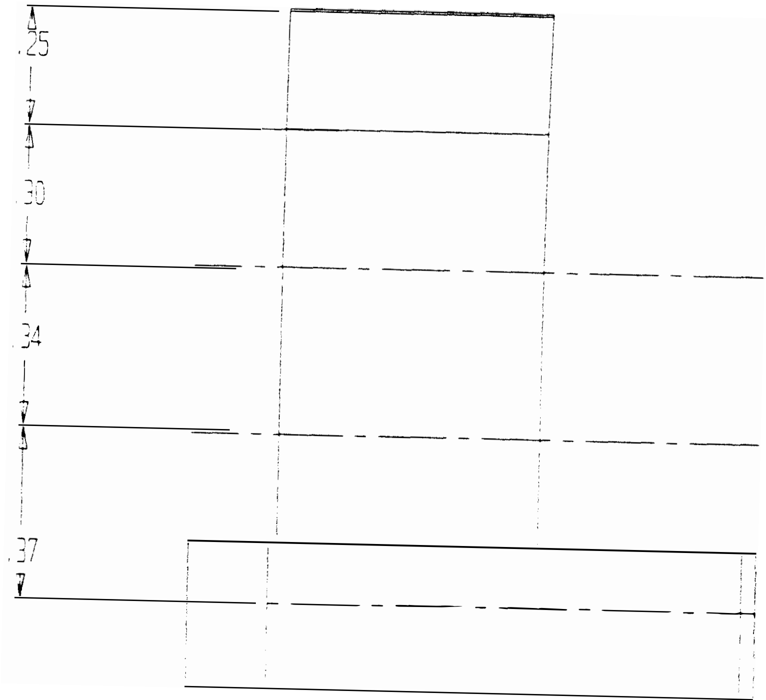

Figure A2.5 Workpiece holder

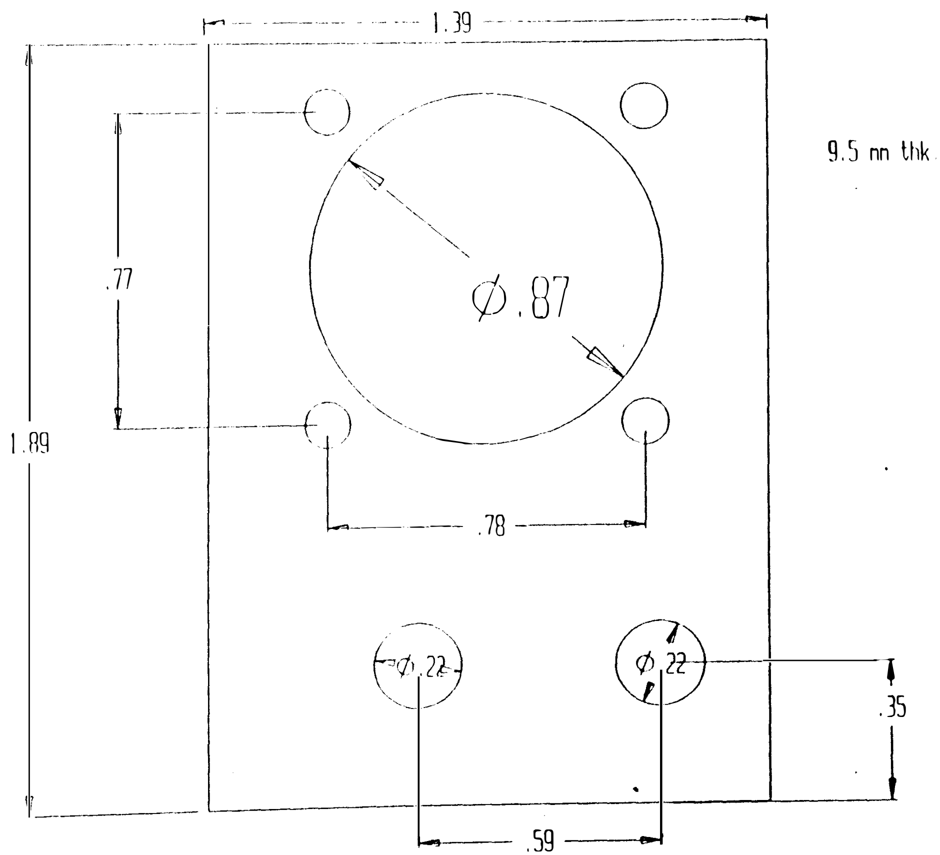

Figure A2.6. Ball screw assembly mounting plate

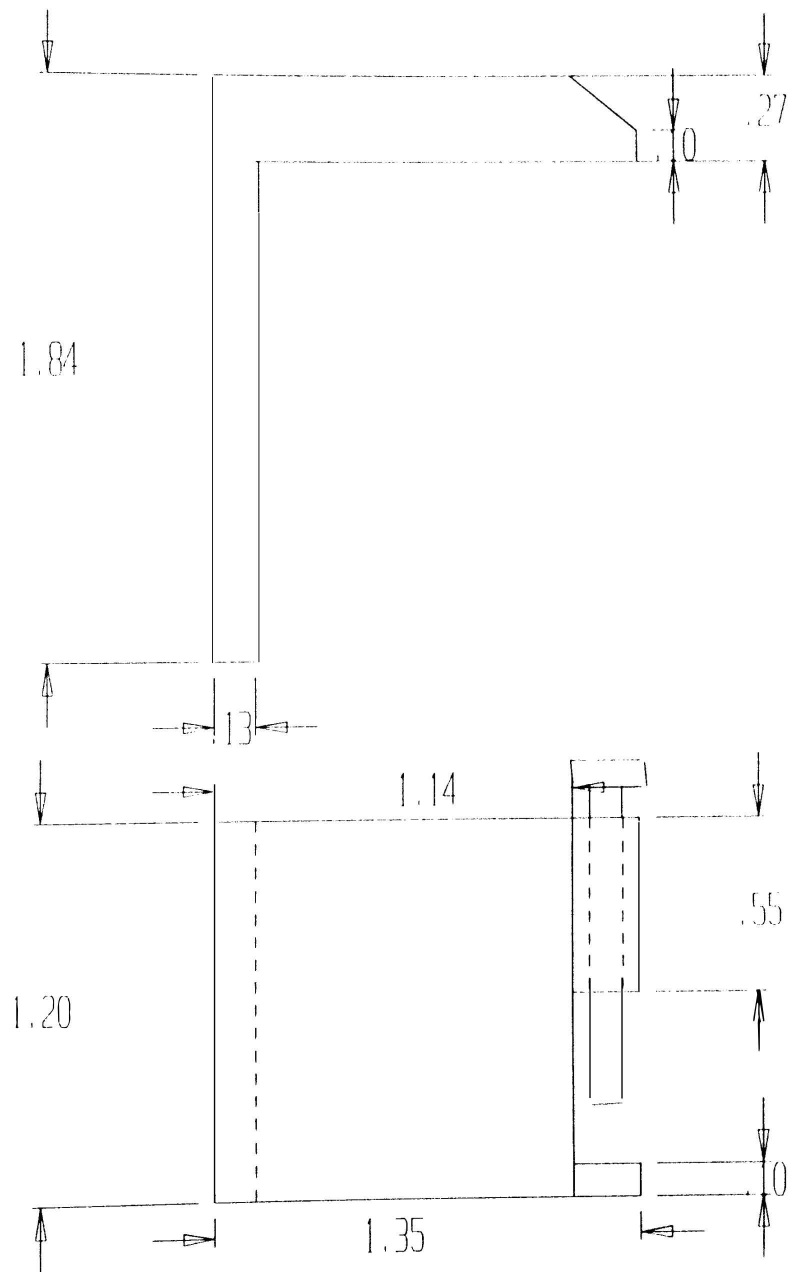

Figure A2.7. Tool holder for third design

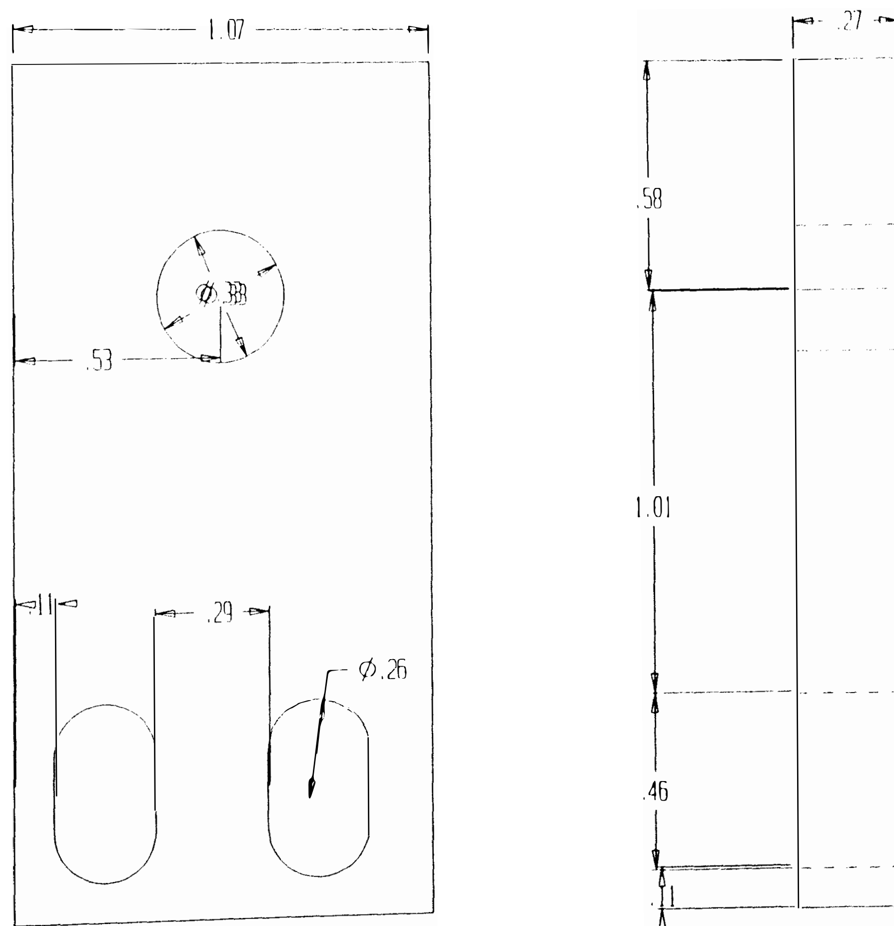

Figure A2.8. Piezo mount

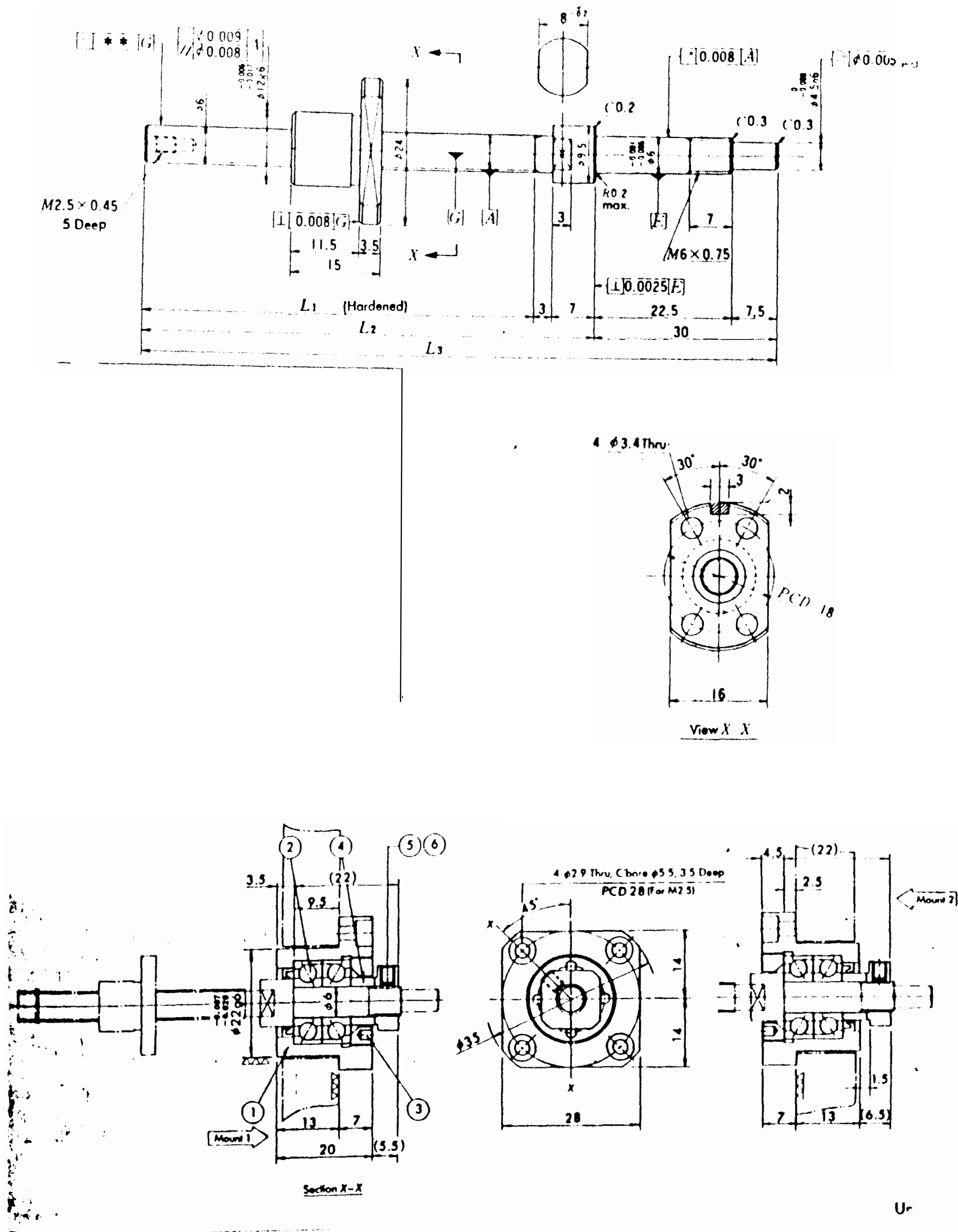

Figure A2.9. Ball screw assembly. (a) precision ball screw assembly (b) Flange type support unit

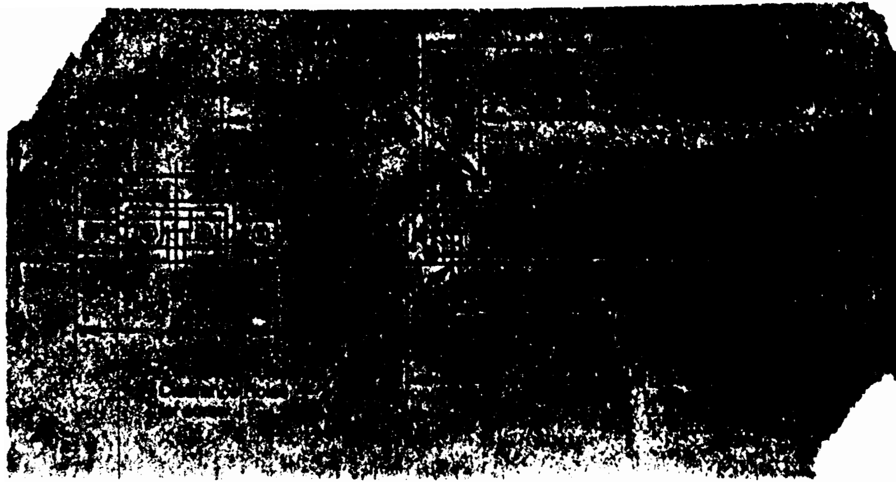

Figure A2.10 Ultraprecision linear slide

Piezo Translator with Position Sensor

A piezo translator is an electrically controllable positioning element which function on the principle of piezo electric effect .Extremely fine positioning movements in the range from nanons to microns is possible. The principle of a piezo translator is, an electric field, parallel to the direction of polarization, effects an expansion of the ceramic material in the same direction .The electric field exercises a torque on the aligned dipole.This torque causes change in length in the monocrystalline region .The active part of the positioning element consists (Figure A2.11) of a thin stack of thin ceramic disks between which are found flat metallic electrodes to feed in the operating voltage. Each ceramic disk lies between two electrode surfaces, one of which is connected to control voltage and another to ground.The thinner the disk, the higher the field strength and therefore the relative change in length for a given operating voltage .The disk thickness varies from 0.3 to 1 mm.The individual disks and electrodes are connected to each other with epoxy cement and hermetically sealed on the outside with highly insulating material. The materials used are sintered ceramics such as lead zirconium titanate compounds. The expansion of the PET depends on the applied voltage.

Application in Vacuum: When using PET in Vacuum it should not be operated between 0.01 torr to 10 torr because air in the above mentioned pressure range has a low insulation resistance, in which voltage spark over may occur. ESEM is generally operated in 5 to 10 torr range so care should be taken to operate it above 10 torr.

Position Sensor: Four strain gages are attached to the ceramic stack in a full bridge circuit .The achievable positioning accuracy is 0.2% of the nominal expansion.

TABLE A2.1 Specifications of piezo translator

Nominal voltage, volts	-1000
Max.operating voltage, volts	-1500
Polarity	Negative.
Max pushing force, N	1000
Max. pulling force, N	300
Temperature range, °C	-40 to 80°
Electrical connector	SMC
Nominal Expansion, microns	10
Maximum expansion, microns	15
Resonant frequency, KHz	16

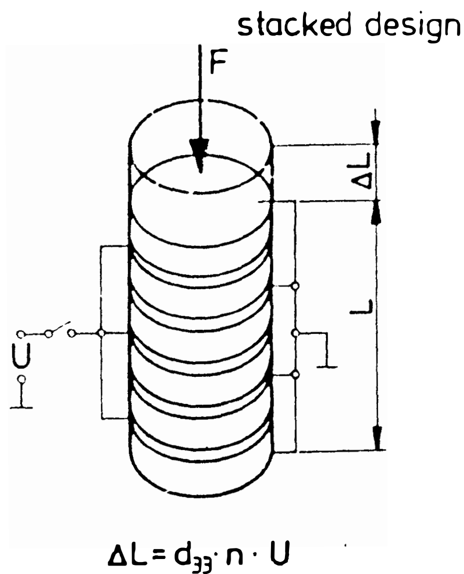

Figure A2.11 stacked design of PZT

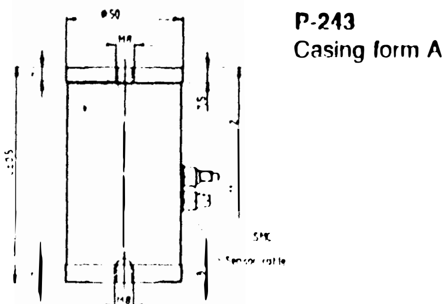

Figure A.2.12 PZT outer casing dimensions [28]

Piezo controller

The expansion of the piezo actuator is controlled by the piezo controller [29]. Technical specifications of the controller is listed in table A2.2.

TABLE A2.2 Specifications of piezo controller

Out put voltage, volts	0 to -1000
Avg. output current, mA	13
Max . output current, mA	50
Input voltage, volts	0 to 10
Input impedance, megaohm	1
Control accuracy, %	better than 0.2
Linearity error, %	< 0.2

Three axis piezoelectric dynamometer

The principle of dynamometer is the evenly distributed force to be measured acts simultaneously upon six washers, electrostatic charges which are exactly proportional to the force exerted and are not dependent on the size of the quartz washers. Of the six inbuilt quartz washers, two each are provided for a specific direction of force Two of them are sensitive to compression only, and the remaining four solely to shearing forces; the sensitive axis of the two pairs forming an angle of 90 degrees. The resultant charges are picked up by the electrodes E and led to the three plug connectors S depending on the direction of the force, the charges produced are either positive or negative. Negative charges give rise to positive voltages at the amplifier output.

It is apparent from figure A2.13 that quartz washers are mounted as a package and are, therefore, mechanically connected in series. Thus, a force will act simultaneously on all of them .In order to enable

tensile and shearing forces-in addition to the compression forces to be measured, the element must be preloaded. The three component measuring element in its finished form is hermetically welded and the plug connectors can be sealed by a thermo shrink sleeve.

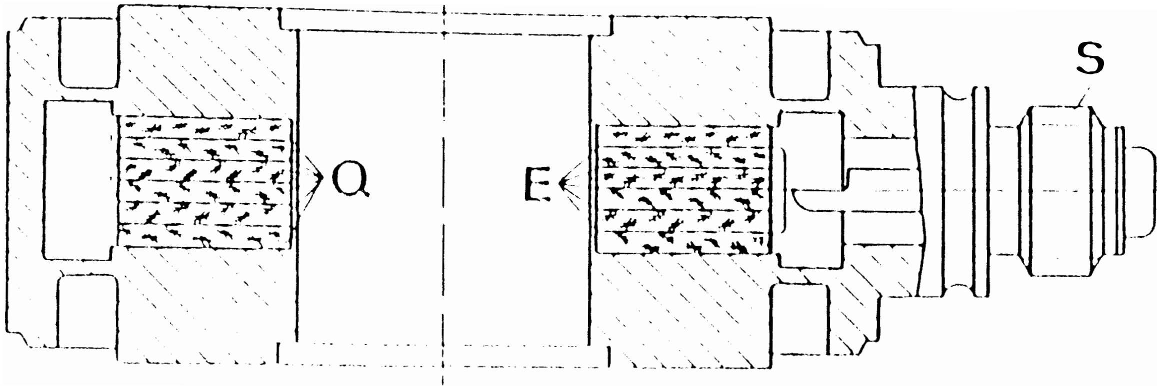

Figure A.2.13. schematic cross section through a 3 - component force measuring element [29]

Application of force

When stiff surfaces lie upon one another, even the smallest asperities give rise to very substantial overloads, to avoid such overloads, the contacting surface of the measuring element is smoothly machined and the contacting surface of the object being measured should be equally plane and smooth. For the element to perform at its best, the force should be applied so as to be uniformly distributed over its contacting area, and bending moment and torque should be avoided when using a single element only , the point of application of the force should not be located too high above the element, in order to preclude the risk of excessive bending moments as seen in Figure A2.15.

Range selection and resolution

Even though a built in measuring element might be subjected to a high static load, it will still enable a very small variation in dynamic force to be measured very accurately as illustrated in the Figure A2.14.

Table A2.3 Specifications of dynamometer

Measuring range with an external pre load of 2500Kp :	
Compression (+) and traction (-) in Z axis, Kp	-500 to + 500
Shearing force (in x and y axis), Kp	-250to+250
Resolution, Kp	0.001
Overload capacity, %	20
Sensitivity (compression and traction), pC/Kp	41
Sensitivity (shearing force), pC/Kp	75 pC/Kp
Stiffness in Z direction, Kp/micron	100
Stiffness in x and y direction, Kp/micron	30
Maximum error, %	+ or - 1
Cross interference of components	<5%
Operating temperature range, °C	- 60 to 250
Max allowable torque, mKp	1.5
Max. allowable bending moment. mKp	1.0
Weight, gms	32 gms
Material	Stainless steel
Design	Hermetically welded

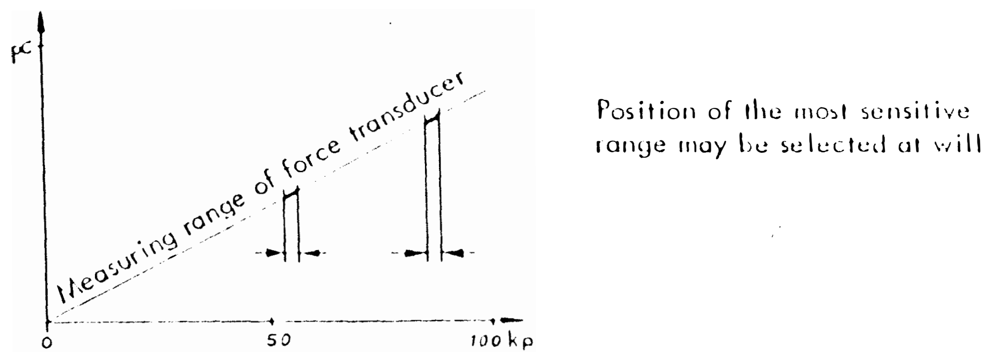

Figure A.2.14 Graphical representation of range selection and resolution [29]

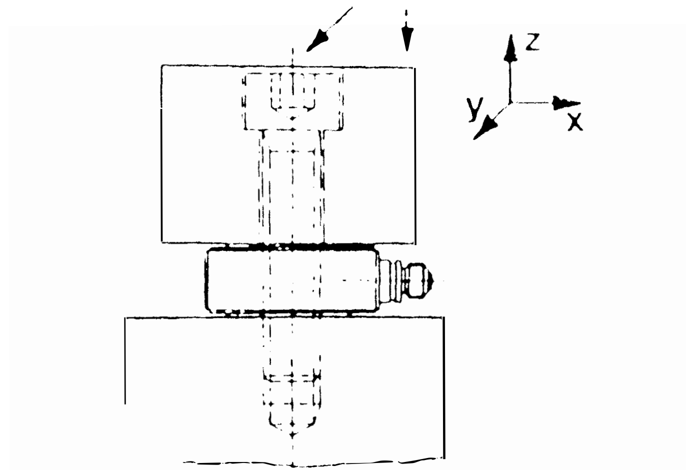

Figure A2.15 . Diagram illustrating the application of force [29]

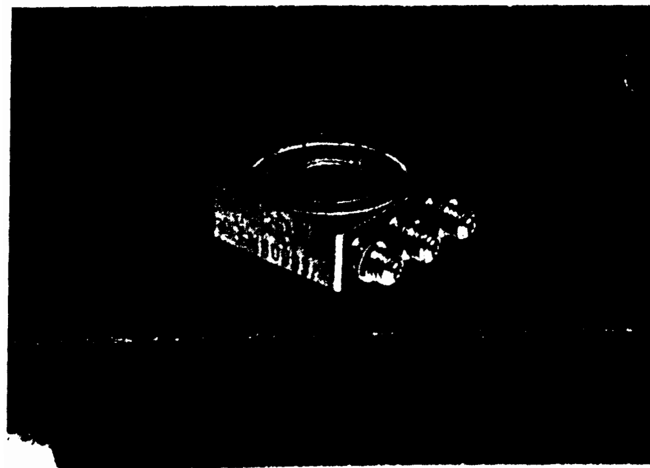

Figure A2.16 . Diagram of force measuring element [29]

Charge amplifier

The out put from the dynamometer cannot be measured directly, it is input into a charge amplifier. The principle of operation is, the charge applied is converted by a first stage with with capacitive feed back into a proportional voltage. Final scaling of the signal for the voltage output takes place in the amplifier.

Ultra precision linear slide

Figure A2.10 [31] illustrates the ultra precision linear slide. It is mounted on the base plate and it guides the work mount precisely in a straight line.

Table A2.4 Specifications of ultraprecision linear slide

Straightness of travel, in/in	0.00004
Repeatability of travel, in	0.00005 in
Life, cycles	10×10^{6}
Rated load, lb	8 Lbs
Material	Black Anodized Aluminum

Precision ball screw assembly

Consists of two units namely standard precision ball screw (Figure A2.9 a) and Flange type support unit (Figure A2.9 b) [32].

Table A2.5 Specifications of precision ball screw assembly

Lead, mm	1
B.C. D, mm	6.2
Lead angle of B.C. D.	2 deg 56 min.

Table A2.5 - continued

Direction of turn	Right
Ball dia, mm	0.8
Number of circuits	1 turn x 3 circuits
Load, dN	60
Axial clearance	0.005 max.
Preload torque, daN-cm	0.15
Stroke length, mm	40

A-11 DC Motor

The dc motor used is of geared type, and measures 1.5 in long and 1 in diameter. The maximum attainable speed is 36 rpm at a maximum of 12 volts supply. The motor produces a continuous torque of 48 oz/in [33]. Figure A2.17 illustrates the speed of carriage (workpiece holder) verses applied voltage to motor.

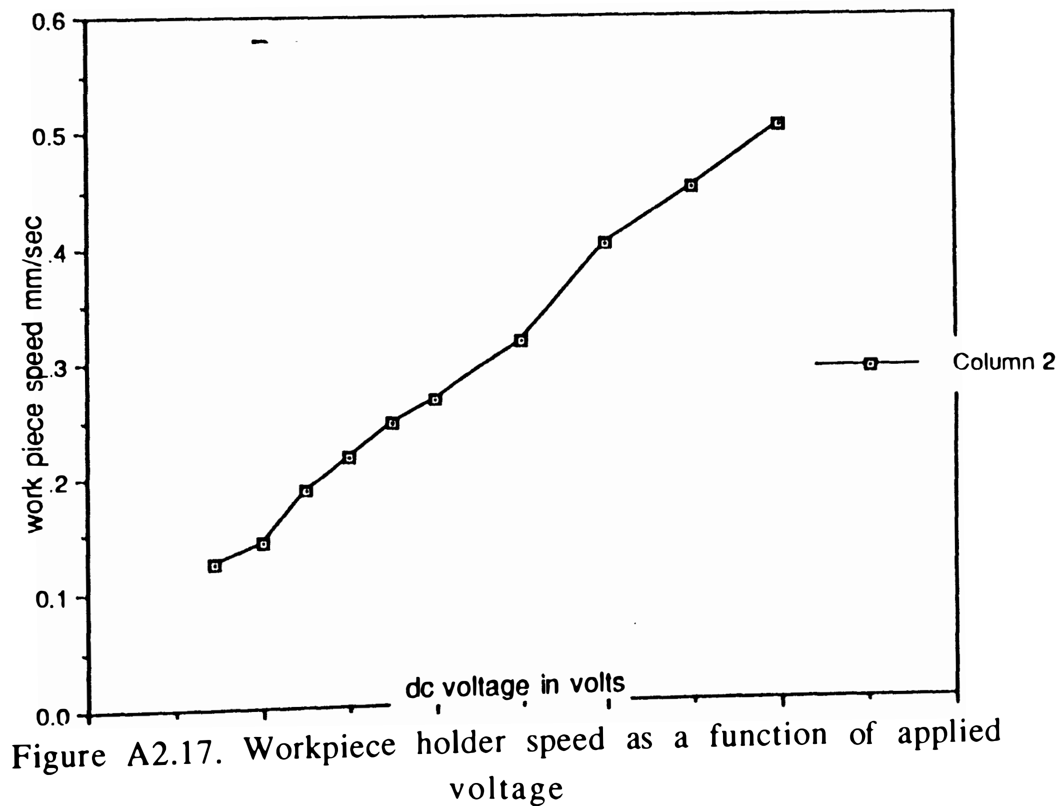

Figure A2.17. Workpiece holder speed as a function of applied voltage

VITA

SANJAI SRIRANGAPATANA KESHAVAN

Candidate for the Degree of

Master of Science

Thesis: AN IN-SITU SCRATCHING STAGE INSIDE ESEM AND ON SCRATCHING OF GLASS

Major Field: Mechanical Engineering

Biographical

Personal Data: Born in Holenarsipur, Karnataka, India, April 10 th, 1969, the son of S. Keshavan and A. R. Amruthamma.

Education: Received Bachelor of Engineering degree in Mechanical Engineering from Mysore university, Karnataka, India in December 1990. August 1992; Completed requirements for the Master of Science degree in Mechanical Engineering, Oklahoma State University, Stillwater, Oklahoma, December 1994.

Professional Experience: Inspection Engineer, UHDE INDIA LTD., Bombay, India, May 1991 to July 1992. Research Assistant, Department of Mechanical Engineering, Oklahoma State University, August 1992 to December 1994.